INTERNATIONAL JOURNAL FOR NUMERICAL AND ANALYTICAL METHODS IN GEOMECHANICS
Int. J. Numer. Anal. Meth. Geomech. (2010)
Published online in Wiley InterScience (www.interscience.wiley.com). DOI: 10.1002/nag.881

Constitutive approach for rate-sensitive anisotropic structured clays

Sean D. Hinchberger[1,*,†,‡], Guangfeng Qu[1,§] and K. Y. Lo[2,¶,‖]

[1]*Department of Civil and Environmental Engineering, University of Western Ontario, London, Ont., Canada N6A 5B9*
[2]*University of Western Ontario, London, Ont., Canada N6A 5B9*

SUMMARY

This paper describes a constitutive approach to model the behavior of rate-dependent anisotropic structured clay. Rate-sensitivity is modeled using overstress viscoplasticity. Clay structure is treated as a viscous phenomenon whereby the viscosity of the undisturbed structured clay is initially very high and the viscosity degrades or decreases with plastic straining until the intrinsic or residual viscosity is reached. A microstructure tensor approach is used to make the structured viscosity anisotropic; whereas, the intrinsic viscosity is assumed to be isotropic. The behavior of the constitutive model is compared with the measured response of two clays (Gloucester and St. Vallier clay) from Eastern Canada during triaxial compression tests on specimens trimmed at different orientations to the vertical. The comparisons show that the constitutive framework is able to describe the anisotropic and rate-sensitive response of both clays. The response of the model is also examined for the more general case of anisotropic consolidated triaxial compression and extension. Copyright © 2010 John Wiley & Sons, Ltd.

Received 4 March 2009; Revised 17 October 2009; Accepted 9 November 2009

KEY WORDS: elastic–viscoplastic; anisotropic; microstructure; microstructure tensor; overstress viscoplasticity; viscous effects

1. INTRODUCTION

Soft clay deposits are widely distributed throughout the world, and consequently, many countries build infrastructure on or in these difficult soils. During loading, undisturbed clay can exhibit

*Correspondence to: Sean D. Hinchberger, Department of Civil and Environmental Engineering, University of Western Ontario, London, Ont., Canada N6A 5B9.
†E-mail: shinchberger@eng.uwo.ca
‡Associate Professor.
§Research Assistant.
¶Professor Emeritus.
‖Director of the Geotechnical Research Center.

Contract/grant sponsor: Natural Sciences and Engineering Research Council of Canada

engineering characteristics such as rate-sensitivity, drained and undrained creep, accelerated creep-rupture and anisotropy [1–4]. Many of these characteristics have been attributed to microstructure or structure, which refers to the effects of fabric and weak bonding between clay particles [5]. Furthermore, Leroueil and Vaughan [6] and Burland [7] have noted that structure has as much influence on the engineering behavior of clay as other state variables such as void ratio and stress history.

This paper describes a constitutive approach to model the time-dependent anisotropic behavior of rate-sensitive structured clay at yield and failure. First, the paper summarizes the engineering characteristics that are modeled. Then, an existing isotropic elastic–viscoplastic (EVP) constitutive model [8, 9] is extended to include the effects of structure and anisotropy on the yielding and failure of high void ratio clays with liquidity indices, LI, near or greater than one. The new constitutive model utilizes non-linear elasticity theory, Perzyna's [10] theory of overstress viscoplasticity, a Drucker–Prager envelope, and an elliptical cap [11] yield surface. Structure is treated as a viscous phenomenon by adopting a viscosity parameter, which is initially high and that decreases to the residual or intrinsic viscosity due to plastic strain [12]. The initial structured viscosity is made anisotropic using a tensor approach similar to that described by Boehler [13], Pietruszczak and Mroz [14] and Cudny and Vermeer [15]; whereas, the intrinsic viscosity is assumed to be isotropic. Finally, the theoretical response of the model is compared with the measured response of Gloucester clay [16] and St. Vallier clay [2] corresponding to constant rate-of-strain (CRS) triaxial compression tests on specimens trimmed at different orientations to the vertical. The response of the model is also examined for the more general case of anisotropic consolidation followed by undrained CRS triaxial compression and extension. The following sections illustrate a simple constitutive approach capable of accounting for the influence of structure and strain-rate on the engineering response of clays that exhibit rate-sensitivity and pronounced destructuring during loading.

2. ENGINEERING BEHAVIOR CONSIDERED

The influence of structure is typically deduced by comparing the response of undisturbed clay during loading to the response of the corresponding reconstituted or destructured material [7]. For example, Figure 1 compares the behavior of undisturbed and destructured Rosemére clay [17] during isotropic consolidated drained (CID) triaxial compression tests. The influence of structure is illustrated by the hatched area in Figure 1. For Rosemére clay, structure imparts additional strength and stiffness to the soil skeleton above that of the corresponding remolded or destructured clay.

Figure 2 compares the corresponding response of Nicolet clay [17] during CID triaxial compression tests and CID triaxial creep tests. Figure 2(a) plots deviator stress, q, versus axial strain corresponding to CID triaxial compression; whereas, Figure 2(b) summarizes axial strain versus time during drained creep at constant deviator stresses of 74 and 54 kPa, respectively. The large-strain post-peak strength for the tests in Figure 2 is 54 kPa. As shown in Figure 2, the additional strength imparted by structure is metastable resulting in: (i) the specimen reaching a peak strength followed by significant post-peak strength loss with large-strain (Figure 2(a)) and (ii) creep-rupture at constant deviator stresses that exceed the large-strain post peak strength of the material (Figure 2(b)).

In addition, most clays exhibit time dependency and rate-sensitivity during drained and undrained loading. It is widely recognized [18, 19] that both the undrained shear strength, s_u, and

DOI: 10.1002/nag

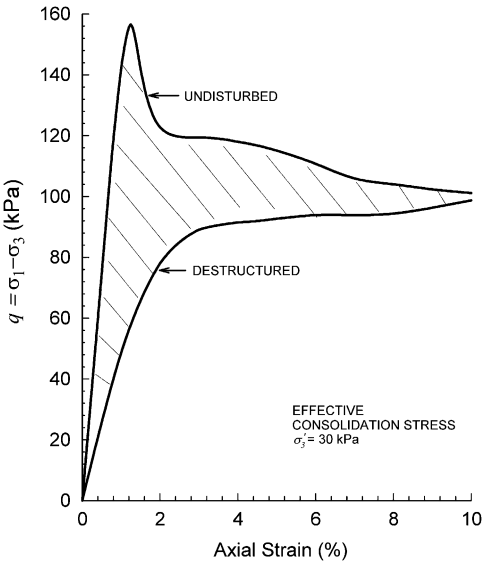

Figure 1. Structured and destructured stress-strain response of Rosemére clay during CID triaxial compression (adapted from [17]).

preconsolidation pressure, σ'_p, of clay increase by 5–15% per order of magnitude increase in strain-rate. Figure 3(a) illustrates the effect of strain-rate on the stress-strain response of Belfast and Winnipeg clays [19–22] and Figure 3(b) summarizes the influence of strain-rate on the undrained shear strength of both clays corresponding to axial strains of 1.8, 10 and 15% [22]. Referring to Figure 3(b), it can be seen that there is a linear variation of mobilized shear strength versus strain-rate when plotted on a log–log scale. Such behavior can be described using a power law [21, 22]. In addition, the rate-sensitivity, which is characterized by the slope α in Figure 3(b) is the same at the peak strength and large-strain post-peak strength corresponding to axial strains of 10 and 15%.

Adding further complication, the undrained shear strength of clay is typically anisotropic [2, 16, 23] and [24]. To illustrate this, Figure 4(a) shows the stress-strain response of Gloucester clay obtained by performing CIU triaxial compression tests on specimens trimmed at various angles, i, relative to vertical [16]. Figure 4(b) shows the corresponding effective stress paths and Table I summarizes details for these tests. Referring to Figure 4(a), the peak undrained strength of Gloucester clay varies with the specimen orientation. In contrast, the large-strain post-peak strength is essentially independent of i. Inspection of the effective stress paths in Figure 4(b) indicates that all specimens reach the same critical state line denoted by M_c at large-strain, which is also independent of the sample orientation, i. Similar behavior has been reported for other Eastern Canadian clays such as Heron Road clay [16] and St. Vallier clay [2].

To conclude, Figure 5(a) and (b) show the influence of structure on the yield surface and compressibility of St. Alban clay [25]. Curve I in Figure 5(a) corresponds to undisturbed St. Alban clay. The yield stresses associated with Curve I were determined from a series of drained and undrained triaxial probes on undisturbed specimens. Curve II in Figure 5(a) corresponds to the yield surface of destructured St. Alban clay. Destructured clay was obtained by anisotropically

DOI: 10.1002/nag

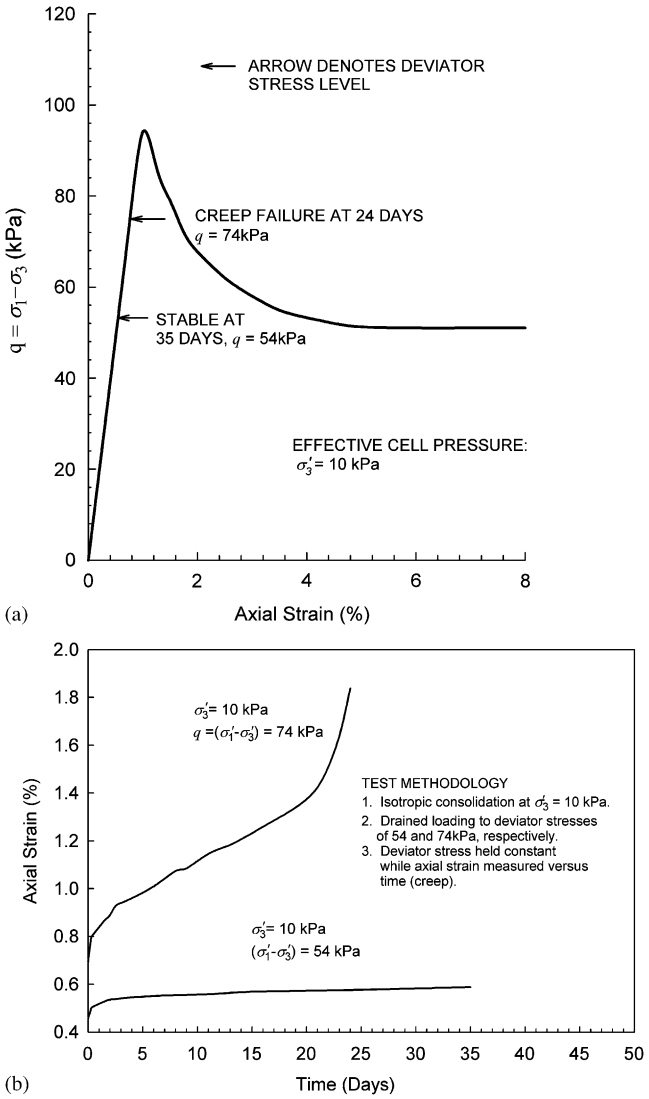

Figure 2. Drained stress-strain-time response of Nicolet clay from Eastern Canada (adapted from [17]). (a) Peak, post-peak response during CID triaxial compression and (b) Creep-rupture during CID triaxial creep tests.

consolidating specimens ($K_o = 0.5$ and 0.6) to induce high volumetric strain (8–14%). Then, the specimens were unloaded (also $K_o = 0.5$ and 0.6) and subsequently re-loaded using drained and undrained triaxial probes to measure the destructured yield stress. Figure 5(b) shows the corresponding response during CRS oedometer compression where it can be seen that St. Alban clay reaches the intrinsic state at about 20% volumetric strain.

DOI: 10.1002/nag

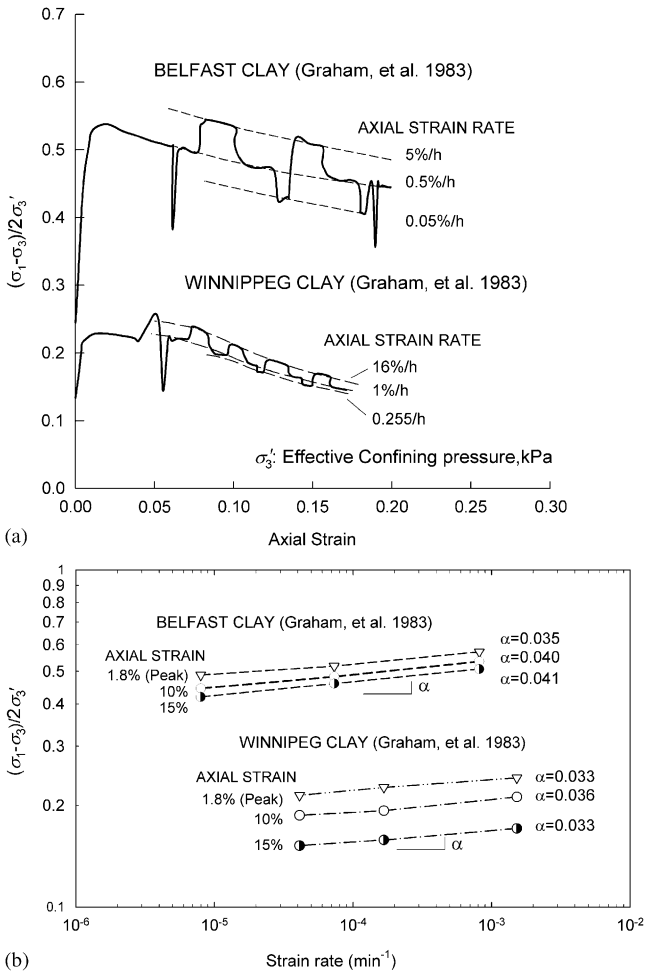

Figure 3. The effect of strain-rate on the undrained shear strength of Belfast and Winnipeg clays (adapted from [19] and [21]). (a) CAU triaxial compression tests with strain-rate changes and (b) Variation of undrained shear strength with strain-rate and strain.

Referring to Figure 5(a), it can be seen that the structured yield surface of St Alban clay (Curve I) is anisotropic and it appears to be rotated about the K_o- line on the $\sigma'_m - \sqrt{J_2}$ plane. In contrast, the destructured yield surface (Curve II) is much less anisotropic and an elliptical cap [11] that is centered on the σ'_m-axis of the $\sigma'_m - \sqrt{J_2}$ plane can be fit through the yield points with less than 10% error. For St. Alban clay (LI$=2.7$), the influence of destructuration overshadows the effects of induced anisotropy for the K_o-conditions examined ($K_o = 0.5 - 0.6$). Such a behavior is likely due to the high void ratio (2.4) of St. Alban clay. Similar behavior has been observed for St. Vallier clay and St. Louis clay [2, 6], Atchafalaya clay [6], Bothkenar clay [26] and Onsøy clay [27].

In summary, the response of rate-sensitive structured clay is complex. The behavior is often characterized by: (i) specimens that reach a peak strength during triaxial compression followed by

DOI: 10.1002/nag

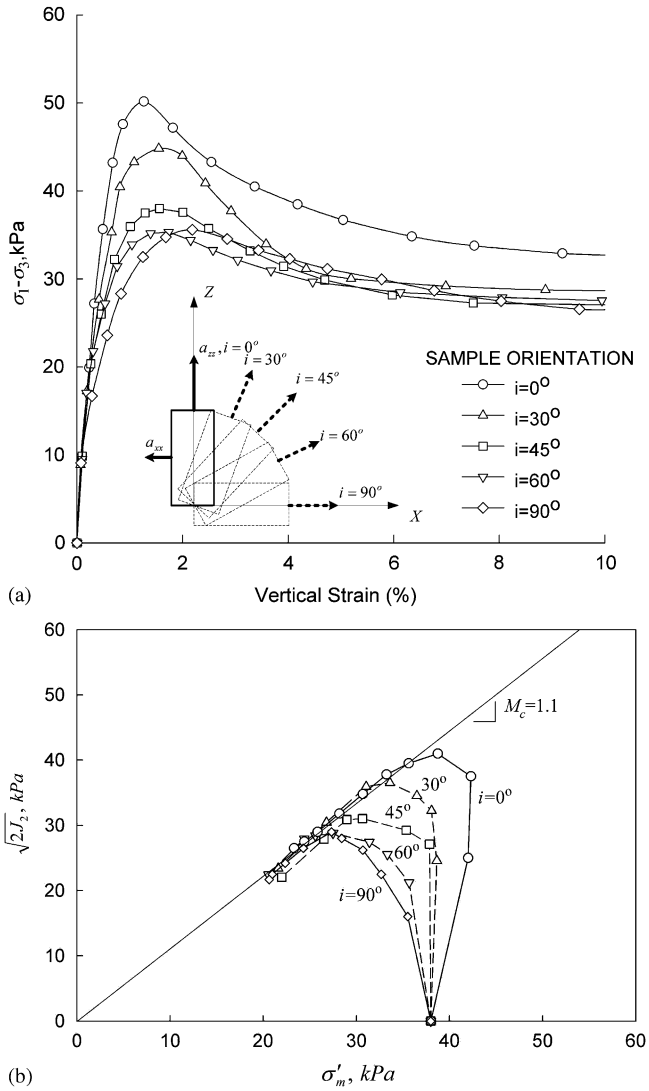

Figure 4. The effect of sample orientation, i, on the response of Gloucester clay during CIU triaxial compression tests [16]. (a) Stress-strain response and (b) Corresponding effective stress paths.

significant post-peak strength loss [1–3, 16] and [17], (ii) creep-rupture at constant deviator stresses exceeding the large-strain post-peak strength of the material [1, 3, 17, 28, 29], (iii) rate-sensitivity [1, 2, 18, 30] and (iv) a structured yield surface that is rotated about the K_o- line on the $\sigma'_m - \sqrt{J_2}$ plane and that becomes approximately elliptical and centered on the σ'_m-axis after destructuration [2, 6, 25–27]. The following section describes a simple approach to model these characteristics neglecting induced anisotropy.

DOI: 10.1002/nag

Table I. Summary of triaxial tests on Gloucester clay [16].

Sample Orientation, i (degrees)	Depth (m)	Axial strain-rate (%/min)	Effective consolidation pressure		Moisture content, w_n (%)	Test	Location in this paper
			σ'_1 (kPa)	σ'_3 (kPa)			
0	2.44	0.017	38	38	66.2	CIU	Figures 4 and 12
30					71.6	CIU	
45					67.3	CIU	
60					72.0	CIU	
90					70.3	CIU	
0		0.017	48.3	33.7	65	CAU	Figures 14 and 15
0		0.00092			67.3	CAU	
0		0.00010			65.7	CAU	
0		0.43	NA	NA	73.1	UU	Figure 14
0		0.086			71.9	UU	
0		0.0093			71.8	UU	
0		0.00093			71.5	UU	
0		0.00010			70.5	UU	

Note: UU—unconsolidated undrained, CIU—isotropic consolidated undrained; CAU—anisotropic consolidated undrained.

3. CONSTITUTIVE MODEL

3.1. Hinchberger and Rowe (1998) model [8, 9]

The constitutive model is an extension of the Hinchberger and Rowe model [8, 9], which has a yield surface defined by the elliptical cap [11] yield function and a Drucker–Prager envelope. Figure 6 shows the yield surface and other characteristics of the model, which are summarized below. It is noted that references [31–33] describe other EVP models for clayey soils.

The EVP constitutive equation is

$$\dot{\varepsilon}_{ij}=\dot{\varepsilon}^{e}_{ij}+\dot{\varepsilon}^{vp}_{ij}=\frac{\dot{s}_{ij}}{2G}+\frac{\kappa}{3(1+e)}\frac{\dot{\sigma}'_m}{\sigma'_m}\delta_{ij}+\frac{1}{\mu}\langle\phi(F')\rangle\left[\frac{\partial F}{\partial\sigma'_{ij}}\right] \tag{1}$$

where $\dot{\varepsilon}_{ij}$ is the strain-rate tensor, $\dot{s}_{ij}$ is the deviatoric stress tensor, σ'_m is the mean effective stress ($\sigma'_m=p'=tr(\sigma')/3$), δ_{ij} is Kronecker's delta, G is the stress-dependent shear modulus, κ is the slope of the $e-\ln(\sigma'_m)$ curve in the over-consolidated stress range, e is the void ratio, μ is a phenomenological viscosity parameter, and $\partial F/\partial\sigma'_{ij}$ is the normalized plastic potential assuming associated plastic flow. In the elastic stress range, the material response is assumed to be non-linear elastic ($E=3(1-2v)(1+e)\sigma'_m/\kappa$) according to Modified Cam Clay theory [34, 35]; whereas, the plastic response is assumed to be time-dependent according to Perzyna's [10] theory of overstress viscoplasticity.

DOI: 10.1002/nag

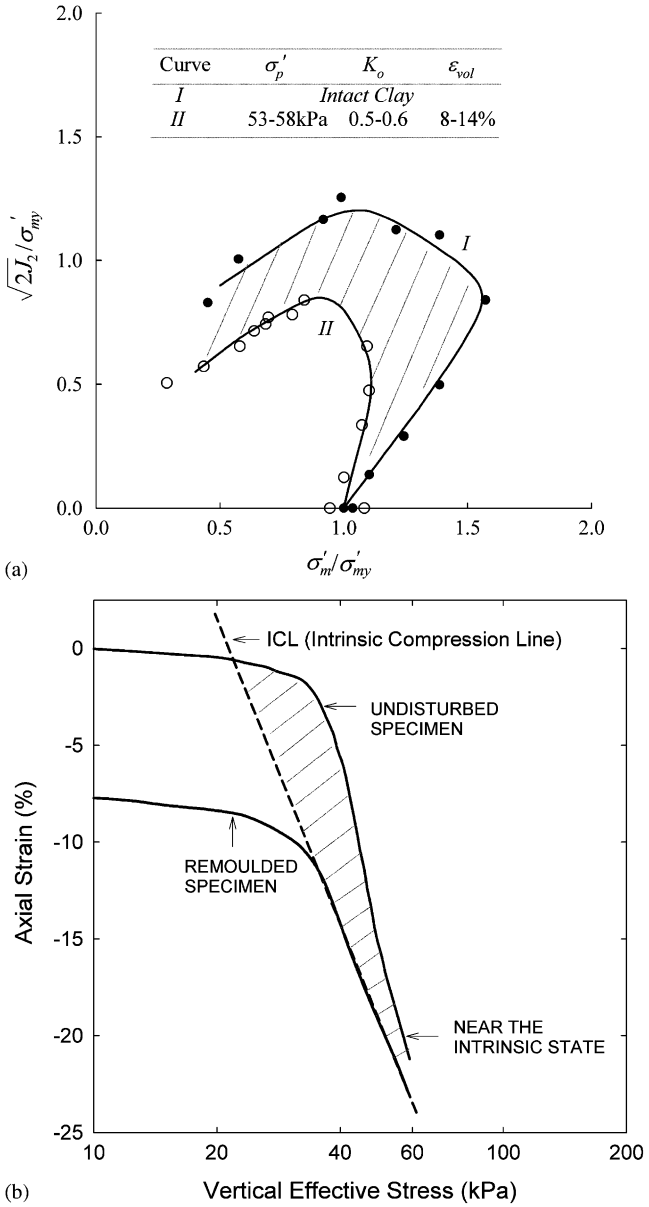

Figure 5. The influence of structure on the yielding of St. Alban clay (adapted from [3, 25]). (a) Normalized yield curves and (b) Structured and intrinsic oedometer compression curves.

Figure 6 shows the modeled yield surface and critical state line on the $\sigma_m' - \sqrt{2J_2}$ plane. First, the critical state line is defined using a Drucker-Prager envelope,

$$F = \sqrt{2J_2} - M_c \sigma_m' = 0 \tag{2}$$

DOI: 10.1002/nag

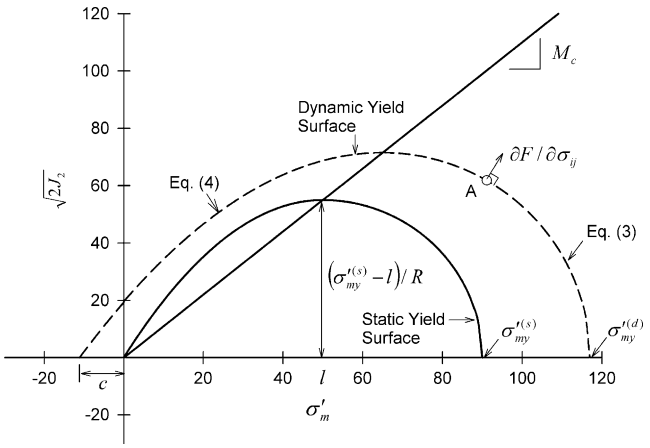

Figure 6. Yield surface, critical state and plastic potential-extended Hinchberger and Rowe model [8].

where J_2 is the second invariant of the deviatoric stress tensor ($J_2 = (s:s)/2$) and M_c is the slope of the critical state line. In relation to the $p'-q$ plane, $\sqrt{2J_2} = \sqrt{2/3}q$, and $M_c = \sqrt{2/3}M$, where $q = \sigma'_1 - \sigma'_3$ and M is the slope of the critical state line on the $p'-q$ plane. In the normally consolidated (NC) stress range, the elliptical cap [11] yield surface is used, viz.

$$F_y = (\sigma'_m - l)^2 + 2J_2R^2 - (\sigma'^{(s)}_{my} - l)^2 = 0, \tag{3}$$

where R is the yield surface aspect ratio (see Figure 6), l and $M_c l$ are the σ'_m- and $\sqrt{2J_2}$-coordinates of the top of the cap, and $\sigma'^{(s)}_{my}$ is the intercept of (3) with the σ'_m-axis. Since, the top of the cap intersects the critical state line represented by (2), then

$$l = \sigma'^{(s)}_{my}/(RM_c + 1). \tag{4}$$

In the over-consolidated (OC) stress range, the yield function [36] is

$$F_y = \sqrt{2J_2} - \alpha(\sigma'_m + c) + \beta(\sigma'_m + c)^2 = 0. \tag{5}$$

where $\alpha = 2M_c l/(l+c)$, $\beta = M_c l/(l+c)^2$, l is an elliptical cap parameter and c is shown in Figure 6. Equations (3)–(5) define a continuous yield surface in $\sigma'_m - \sqrt{2J_2}$ stress space that is assumed to harden isotropically due to plastic volumetric strain, $\varepsilon^{vp}_{\text{vol}}$, viz.

$$\partial\sigma'^{(s)}_m = \frac{(1+e)}{(\lambda-\kappa)}\sigma'^{(s)}_{my}\partial\varepsilon^{vp}_{\text{vol}} \tag{6}$$

In the EVP model, a static or reference yield surface is used to define the transition from rate-independent elastic behavior to rate-dependent viscoplastic behavior. The static yield surface is defined using (3)–(5) corresponding to $c = 0$ and the isotropic yield stress, $\sigma'^{(s)}_{my}$. The superscript (s) denotes the static yield surface. Unlike plasticity theory, however, the stress state in EVP theory is permitted to exceed the static yield surface as depicted by Point A in Figure 6. For Point A, the plastic strain-rate is calculated by defining a dynamic yield surface using (3)–(5) with intercept

DOI: 10.1002/nag

$\sigma'^{(d)}_{my}$ that passes through point A. The superscript (d) denotes dynamic. The corresponding rate of plastic flow is then

$$\dot{\varepsilon}^{vp}_{ij} = \frac{1}{\mu}\langle\phi(F)\rangle\left[\frac{\partial F}{\partial \sigma'_{ij}}\right] \tag{7}$$

where $\phi(F)$ is

$$\phi(F) = \begin{matrix}(\sigma'^{(d)}_{my}/\sigma'^{(s)}_{my})^n - 1 \\ 0\end{matrix} \quad \text{for} \quad \begin{matrix}F>0 \\ F\leqslant 0\end{matrix}. \tag{8}$$

In (8), overstress is defined by the ratio $\sigma'^{(d)}_{my}/\sigma'^{(s)}_{my}$ similar to Adachi and Oka [33] and the exponent n governs the rate-sensitivity of the material. As such, the viscosity parameter, μ, and the power law flow function, $\phi(F)$ govern the plastic strain-rate and the relative magnitude of the principle components of plastic strain are defined by the plastic potential $\partial F/\partial\sigma'_{ij}$, which is derived as a unit vector on the $\sigma'_m - \sqrt{2J_2}$ plane assuming associated flow. Furthermore, from Equations (1)–(8), it can be shown that $\alpha = 1/n = C_\alpha/(C_c - C_r)$, where C_α is the coefficient of secondary compression, and C_r and C_c are from incremental oedometer tests and commonly referred to as the recompression and compression indices, respectively.

Since $\phi(F)$ is a power law, the Hinchberger and Rowe [8, 9] model defines a linear variation of constant volume undrained shear strength, s_u, preconsolidation pressure, σ'_p, and isotropic yield stress, $\sigma'^{(d)}_{my}$, versus strain-rate in log-log space as illustrated in Figure 7. The static yield surface corresponding to Equations (3)–(5) and $\sigma'^{(s)}_{my}$ and the fluidity, μ^{-1}, define the minimum strain-rate for time-dependent behavior (see Points A in Figure 7). For CRS loading, the plastic strains are time-independent if the strain-rate is less than about μ^{-1} and time-dependent if the strain-rate exceeds μ^{-1}. Qu *et al.* [20] summarize the response of 20 clays that exhibit behavior consistent with that depicted in Figure 7. Furthermore, based on data summarized in References [20] and [37], the parameter μ is typically in the order of 10^9s. In the following sections, the model is extended to account for structure and anisotropic structure.

3.2. *Modification for structure* (*Hinchberger and Qu* [*12*])

Burland [7] suggested that the engineering behavior of structured clay can be described with reference to the remolded or intrinsic state. Accordingly, it has been hypothesized in reference [12] that clay structure is a viscous phenomenon that can be defined in terms of the intrinsic and structured viscosities viz.

$$\omega_o = (\mu_s/\mu_i)^{1/n} \tag{9}$$

where ω_o is the initial structure parameter, μ_s is the viscosity of the undisturbed structured clay, μ_s is the viscosity of the clay at the intrinsic state, and n is the power law exponent in (8). The structured soil viscosity is higher than the intrinsic viscosity and consequently $\omega_o \geqslant 1$ (*Note*: the fluidity is $1/\mu$).

Next, the viscosity of the structured clay, μ_s, is assumed to degrade with increasing plastic strain until the intrinsic viscosity, μ_i, is reached. This process is commonly referred to as

DOI: 10.1002/nag

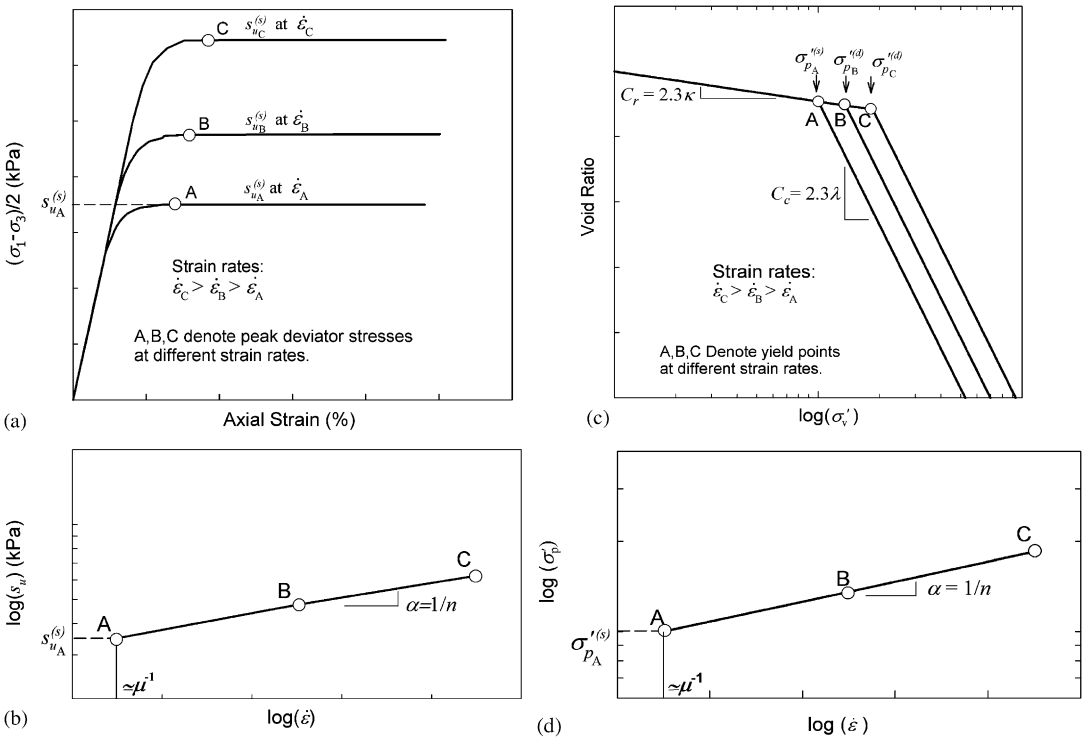

Figure 7. Variation of undrained shear strength and preconsolidation pressure versus strain-rate [20]. (a) Triaxial compression; (b) Undrained shear strength versus strain-rate; (c) Oedometer compression; and (d) Preconsolidation pressure versus strain-rate.

destructuration (e.g. [25, 38] and [39]). In the extended EVP model, destructuration is assumed to occur exponentially as a function of damage strain, viz.

$$\mu(\varepsilon_d) = \mu_i + (\mu_s - \mu_i) e^{-\alpha_d \varepsilon_d} \tag{10}$$

where α_d controls the rate-of-destructuration and the damage strain, ε_d, is from [38]

$$\mathrm{d}\varepsilon_d = \sqrt{(1-A)(\mathrm{d}\varepsilon_{\mathrm{vol}}^{vp})^2 + A(\mathrm{d}\varepsilon_s^{vp})^2}. \tag{11}$$

In (11), A is a weighting parameter (assumed to be 0.5) and $\varepsilon_{\mathrm{vol}}^{vp}$ and ε_s^{vp} are plastic volumetric and octahedral shear strains ($\sqrt{3}\gamma_{\mathrm{oct}}$), respectively. It is noted that, if shear banding (strain localization) is not accounted for in the FE model, then the parameter α_d is higher for stress paths that cause shear failure than for stress paths such as isotropic and K_{o} compression, which cause yielding (see Reference [12]). Incorporating (9)–(11) into the Hinchberger and Rowe [8, 9] model results in an EVP model for structured clay. The viscoplastic strain-rate tensor for such a model is,

$$\dot{\varepsilon}_{ij}^{vp} = \frac{1}{\mu(\varepsilon_d)} \langle \phi(F) \rangle \left[\frac{\partial F}{\partial \sigma'_{ij}} \right]. \tag{12}$$

DOI: 10.1002/nag

Figure 8(a)–(c) illustrates the theoretical behavior of the EVP model during CIU triaxial compression, which is described in this section. First, after isotopic consolidation (see point 1 in Figure 8(a)), CRS triaxial compression will cause the effective stress path to move within the yield surface from point 1 to 2 where first yielding occurs. With continued compression, the structured soil skeleton will undergo time-dependent plastic straining and the stress path will move from 2 to 3 resulting in overstress. However, from points 2 to 3, the plastic strain-rate is negligible due to the high structured viscosity and the resultant material behavior remains essentially elastic (see Figure 8(b)).

At point 3, the overstress and consequent plastic strain-rate are high enough to cause significant destructuring to occur. From point 3 to 4, there is stabilization of the overstress during which the peak strength is reached. From point 4 to 5, the damage rate is high and there is significant reduction of overstress (stress-relaxation) due to shear thinning or degradation of the soil viscosity (see Figure 8(c)). As compression continues, it is assumed that eventually the plastic strain causes the viscosity of the soil skeleton to reach the intrinsic viscosity; although this state may not be reached during triaxial compression.

Figure 9 illustrates the resultant constitutive response for drained CRS oedometer compression and CRS undrained triaxial compression tests. Similar to the unstructured EVP model, there is a linear variation of: (i) peak undrained shear strength, s_{up}, (ii) large-strain post-peak undrained shear strength, s_{u_i}, and (iii) structure preconsolidation pressure, σ'_{ps}, versus strain-rate on a log–log plot. From Equations (1)–(12), it can be shown that the initial structure parameter, ω_o, is approximately equal to

$$\omega_o = s_{up}/s_{u_i}, \tag{13}$$

or

$$\omega_o = \sigma'_{ps}/\sigma'_{pi} \tag{14}$$

where σ'_{pi} is the intrinsic preconsolidation pressure (see Figure 9). Equations (13) and (14) are derived in the Appendix. Clays that behave according to Figure 9 are described in References [1, 19] and [29]. In addition, Reference [12] describes the application of the structured model to St. Jean Vianney clay corresponding to undrained CRS triaxial compression, CRS drained oedometer compression, and undrained constant stress creep-rupture tests.

3.3. Extension for transverse isotropy

If the structure is assumed to be anisotropic, then in accordance with [13–15] and [40], the relative distribution of microstructure can be characterized using a microstructure tensor of the form

$$a_{ij}^T = \begin{bmatrix} 1-\Delta/2 & 0 & 0 \\ 0 & 1-\Delta/2 & 0 \\ 0 & 0 & 1+\Delta \end{bmatrix} \tag{15}$$

where the superscript T denotes transverse isotropy. The parameter Δ is a constitutive parameter that is zero for the case of isotropy and increases as the degree of anisotropy increases. Given (15), the influence of the loading direction relative to the material axes can be taken into account by deriving an anisotropic scalar parameter, η^*, which is obtained by projecting σ'^2_{ij}, onto the microstructure tensor a_{ij}^T. The diagonal components of σ^2_{ij} (L_1^2, L_2^2 and L_3^2) representing the resultant

DOI: 10.1002/nag

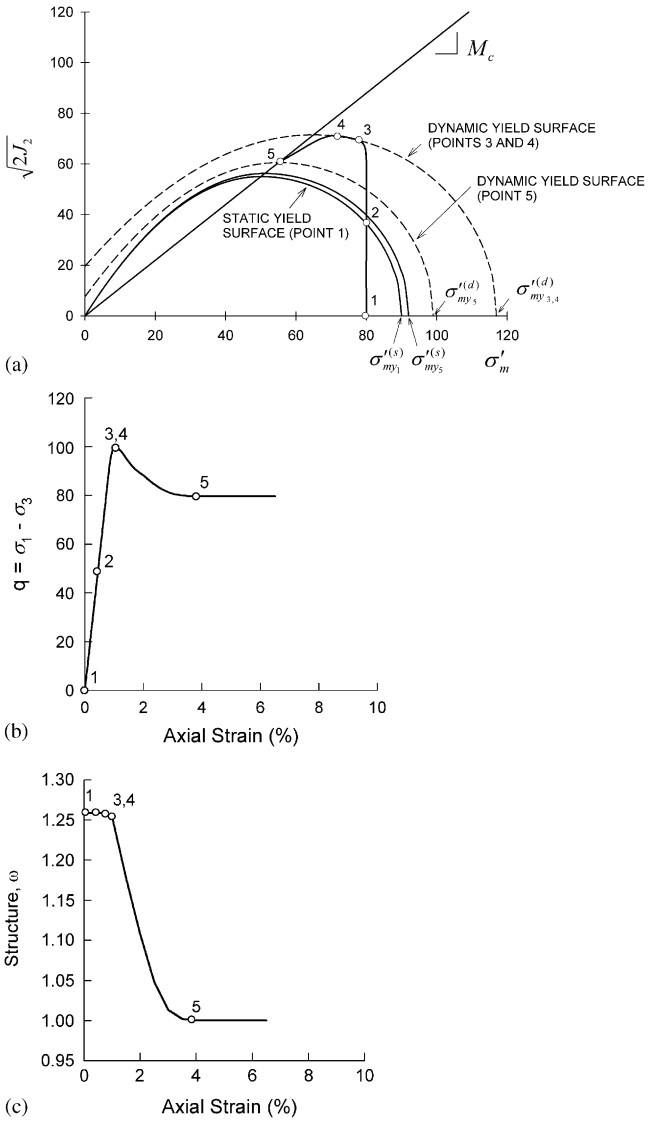

Figure 8. Theoretical response of structured EVP model during CIU triaxial compression. (a) Stress path; (b) Stress-strain response; and (c) Structure parameter.

stresses on each of the principal planes of orthotropy are,

$$\begin{aligned} L_1^2 &= \sigma_{xx}'^2 + \sigma_{xy}'^2 + \sigma_{xz}'^2 \\ L_2^2 &= \sigma_{yx}'^2 + \sigma_{yy}'^2 + \sigma_{yz}'^2 \\ L_3^2 &= \sigma_{zx}'^2 + \sigma_{zy}'^2 + \sigma_{zz}'^2. \end{aligned} \tag{16}$$

DOI: 10.1002/nag

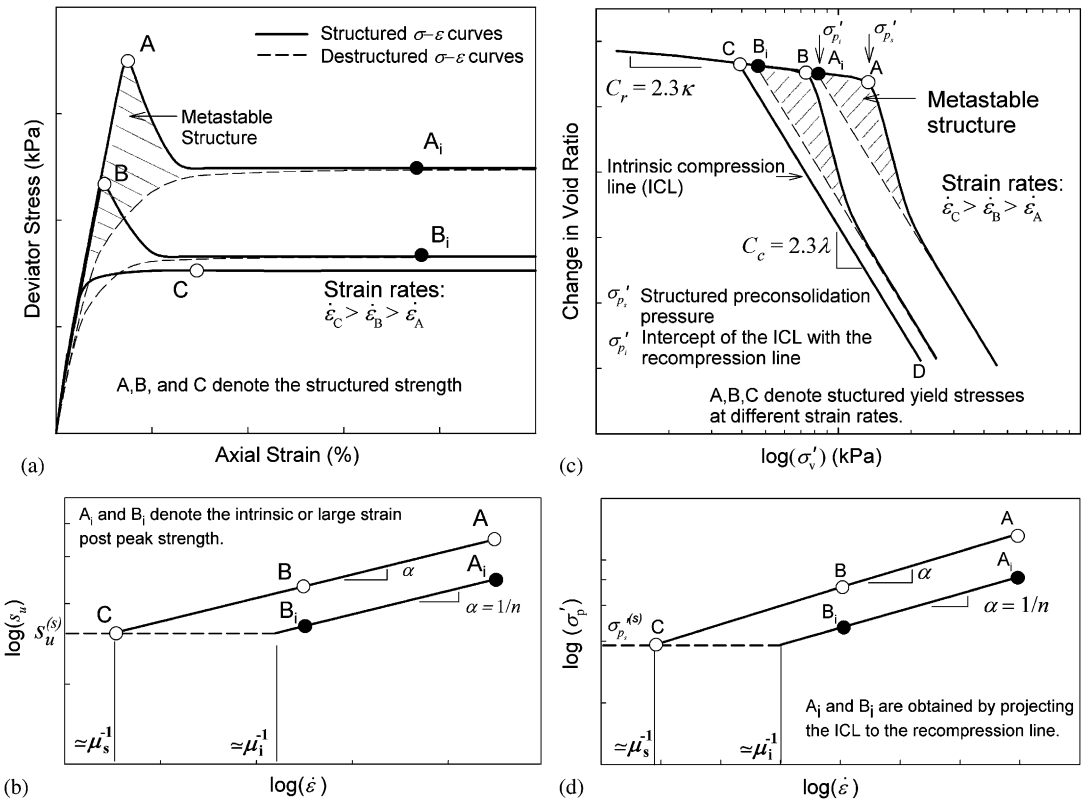

Figure 9. Variation of the undrained strength and preconsolidation pressure versus strain-rate for the structured EVP model [12]. (a) Triaxial compression; (b) Undrained shear strength versus strain-rate; (c) Oedometer compression; and (d) Preconsolidation pressure versus strain-rate.

and the anisotropic scalar parameter, η^*, is

$$\eta^* = tr(\bar{a}_{ij}^T \sigma_{ij}'^2)/tr(\sigma_{ij}'^2) = 1 - \Omega_{ij} l_i l_j \tag{17}$$

where $l_i = L_i/\sqrt{L_1^2 + L_2^2 + L_3^2}$. The average value of η^* is one and the parameter Ω_{ij} defines deviations of η^* from a sphere of unit radius (see Reference [40]). For a vertically orientated ($i = 0°$) specimen subject to an axisymmetric triaxial stress state, (17) simplifies to

$$\eta^* = \frac{\left(1 - \frac{\Delta}{2}\right) L_1^2 + \left(1 - \frac{\Delta}{2}\right) L_2^2 - \Delta L_3^2}{L_1^2 + L_2^2 + L_3^2}. \tag{18}$$

Next, the anisotropic parameter, η^*, can be used to make the initial structure anisotropic, viz.

$$\omega_o(\eta^*) = \eta^* (\mu_s/\mu_i)^{1/n}, \tag{19}$$

DOI: 10.1002/nag

This results in the following state-dependent viscosity

$$\mu(\varepsilon_d, \eta^*) = \mu_i + [(\eta^*)^n \mu_s - \mu_i] e^{-\alpha_d \varepsilon_d}. \tag{20}$$

and the corresponding state-dependent structure parameter is

$$\omega(\varepsilon_d, \eta^*) = (1 + [(\eta^*)^n \mu_s / \mu_i - 1] e^{-\alpha_d \varepsilon_d})^{1/n}. \tag{21}$$

Incorporating Equations (18)–(21) into the EVP model gives an anisotropic structured EVP model with the following viscoplastic strain-rate tensor

$$\dot{\varepsilon}_{ij}^{vp} = \frac{1}{\mu(\varepsilon_d, \eta^*)} \left\langle \left(\sigma_{my}^{\prime(d)} / \sigma_{my}^{\prime(s)} \right)^n - 1 \right\rangle \left[\frac{\partial F}{\partial \sigma_{ij}^{\prime}} \right]. \tag{22}$$

Table II summarizes the extensions made to the Hinchberger and Rowe [8] model.

3.4. Limitations of the model

The primary advantage of the constitutive model described above is its simplicity. However, the simplicity comes with two limitations, which for certain circumstances may be significant if not taken into account. First, the yield surface and failure criterion are isotropic functions with a circular trace on deviatoric planes as depicted by Curve I in Figure 10. In contrast, soils are typically stronger in compression than in extension similar to that depicted by Curve II in Figure 10. The use of a circular trace on deviatoric planes can have implications during the analysis of plane-strain problems where it is well established that using M_c from compression tests ($i = 0^\circ$) in conjunction with a Drucker–prager envelope can lead to over prediction of the collapse height of long embankments by about 15% [41]. The error introduced by this limitation, however, can be minimized if M_c is taken as the average slope of the critical state line in compression and extension (Curve III in Figure 10).

Second, the plastic potential function is also isotropic due to the assumption of normality. As such, although the structured strength in the EVP model is anisotropic, specimens loaded in compression or extension will have the same principle plastic strain-rate directions irrespective of the sample orientation, i. The general implications of this are unknown; however, the laboratory tests examined below in Section 5 are dominated by the model response and clay behavior at or near to critical state corresponding to constant volume shear. As such, the impact of using an isotropic plastic potential function is considered to be insignificant. It is possible to remove the second limitation by modifying the yield surface equations using approaches described in papers [42–48].

4. NUMERICAL PROCEDURES

4.1. Finite element (FE) calculations

This paper compares calculated and measured behavior for Gloucester and St. Vallier clays during CRS triaxial compression tests (CIU) on specimens trimmed at different inclinations, i, relative to the vertical. The triaxial tests were performed on high-quality triaxial specimens trimmed from block samples and using consolidation stresses less than the *in situ* overburden stress. As such, the response is considered to be close to that of the undisturbed structured material. The measured

DOI: 10.1002/nag

Table II. Comparison of elastic–viscoplastic models.

Model	Elastic model	OC yield function, F_y	NC yield function, F_y	Critical state line	Flow function
Hinchberger and Rowe [8]	$K=(1+3v)\sigma'_m/\kappa$, G and v	$F_y\sqrt{2J_2}-M_{oc}\sigma'_m=0$	$F=(\sigma'_m-l)^2+2J_2R^2-(\sigma'^{(s)}_{my}-l)^2=0$	$F=\sqrt{2J_2}-M_c\sigma'_m=0$	$\phi(F)=\frac{1}{\mu}[(\sigma'^{(d)}_{my}/\sigma'^{(s)}_{my})^n-1]$
Hinchberger and Qu [12]	$K=(1+3v)\sigma'_m/\kappa$, G and v	$F_y\sqrt{2J_2}-M_{oc}\sigma'_m=0$	$F=(\sigma'_m-l)^2+2J_2R^2-(\sigma'^{(s)}_{my}-l)^2=0$	$F=\sqrt{2J_2}-M_c\sigma'_m=0$	$\frac{1}{\mu(\varepsilon_d)}[(\sigma'^{(d)}_{my}/\sigma'^{(s)}_{my})^n-1]$
This paper	$K=(1+3v)\sigma'_m/\kappa$, G and v	$F_y=\sqrt{2J_2}-\alpha(\sigma'_m+c)+\beta(\sigma'_m+c)^2=0$	$F=(\sigma'_m-l)^2+2J_2R^2-(\sigma'^{(s)}_{my}-l)^2=0$	$F=\sqrt{2J_2}-M_c\sigma'_m=0$	$\frac{1}{\mu(\varepsilon_d,\eta^*)}[(\sigma'^{(d)}_{my}/\sigma'^{(s)}_{my})^n-1]$

*The hardening law for the cap is $\partial\sigma'^{(s)}_{my}=(1+e)/(\lambda-\kappa)\sigma'^{(s)}_{my}\partial\varepsilon^{vp}_{vol}$ for all models.

DOI: 10.1002/nag

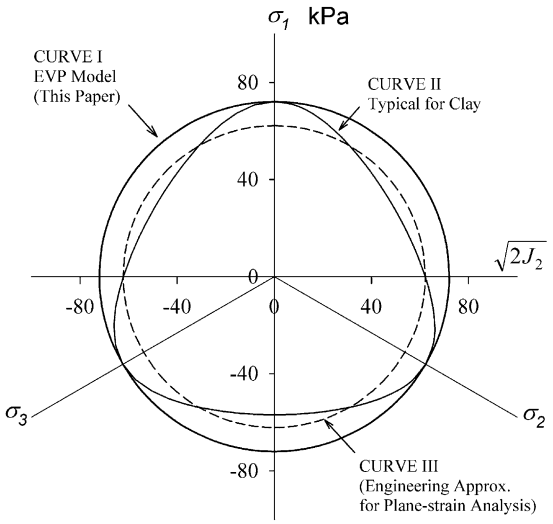

Figure 10. Trace on deviatoric planes.

Table III. Constitutive parameters for Gloucester clay.

Parameter	Value
Initial void ratio, e	1.8
Damage exponent, α_d	0.8
Static yield surface intercept $\sigma_{my}^{\prime(s)}$, (kPa)	48.5
Visoplastic strain-rate exponent, n	30
M_c	1.20
Poisson's ratio, υ	0.3
Recompression index, κ	0.02
Compression index, λ	0.63
Aspect ratio of elliptical cap, R	2.5
A (weighting parameter)	0.5
Δ	0.15
Structured viscosity, μ_s, (s)	9×10^9
Intrinsic viscosity, μ_i, (s)	3.5×10^5

response of Gloucester clay is from Law [16]; whereas, the response of St. Vallier clay comes from Lo and Morin [2]. Both Gloucester and St. Vallier clay were chosen to evaluate the model since these are the only clays reported in the literature that have had tests done to characterize the effects of both strain-rate and sample orientation.

The calculated behavior reported below in Section 5 was obtained using the FE program AFENA [49], which has been modified by the authors to account for time-dependent plasticity and structure. The constitutive parameters, which are summarized in Tables III and IV, were estimated directly from conventional laboratory tests on the corresponding clay. References [12, 20] and [21] describe how to obtain the material parameters. For each triaxial compression test, a FE analysis

DOI: 10.1002/nag

Table IV. Constitutive parameters for St. Vallier clay.

Parameter	Value
Initial void ratio, e	1.6
Damage exponent, α_d	1
Static yield surface intercept $\sigma'^{(s)}_{my}$, (kPa)	70
Visoplastic strain-rate exponent, n	16
M_c	1.85
Poisson's ratio, v	0.3
Recompression index, κ	0.01
Compression index, λ	0.65
Aspect Ratio of elliptical cap, R	1.8
A (weighting parameter)	0.5
Δ	0.3
Structured viscosity, μ_s, (s)	4.2×10^{11}
Intrinsic viscosity, μ_i, (s)	1.0×10^{6}

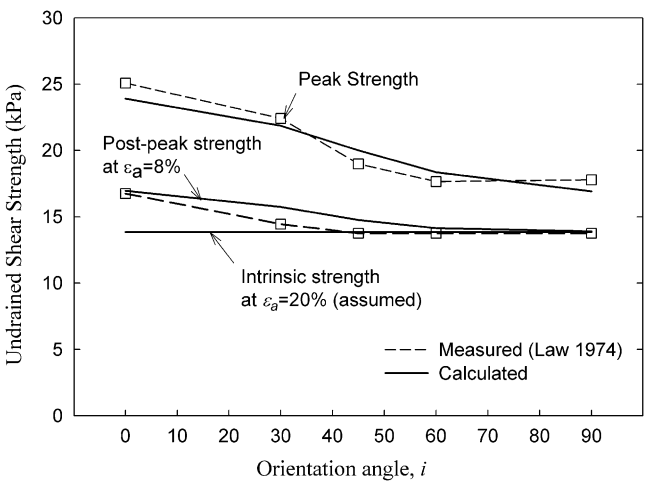

Figure 11. Calculated and measured variation of peak and post-peak undrained shear strength versus sample orientation for Gloucester clay [16].

was performed starting from the stress state after consolidation. The FE mesh comprised 24 6-noded linear strain triangles and calculations were performed assuming axisymmetric geometry. The specimen was loaded by prescribing displacements to the top of the mesh at a rate corresponding to the CRS reported for the test being analyzed. The top and bottom mesh boundaries were assumed to be smooth and rigid (friction was neglected), which resulted in uniform strain in the specimens during simulation of each test. As a result, the strain-softening response given by the model is due entirely to the constitutive parameters as opposed to numerically induced strain localization in the elements. Figures 11–15 summarize the FE calculations for Gloucester clay and Figures 16–19 summarize St. Vallier clay.

DOI: 10.1002/nag

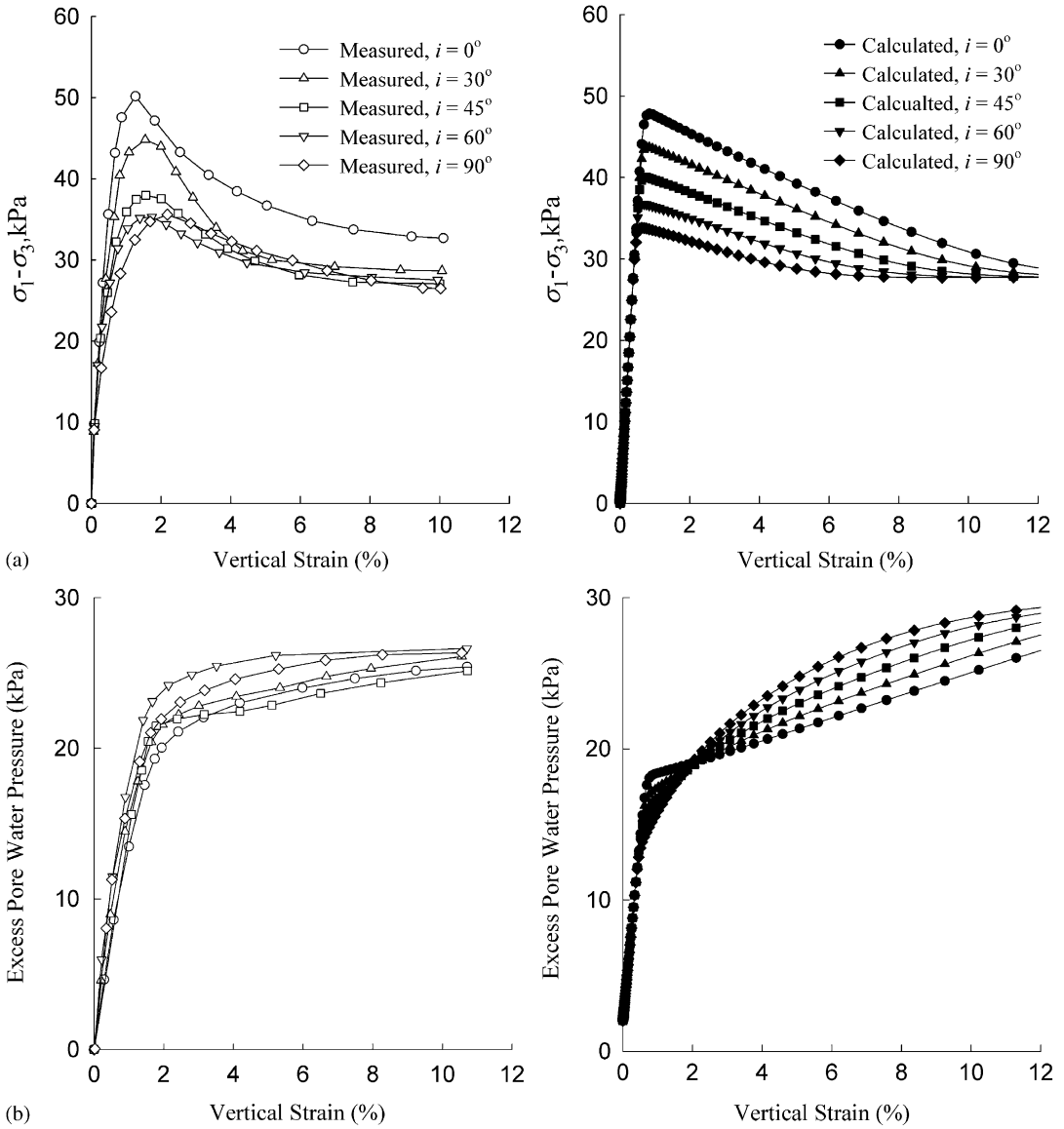

Figure 12. Calculated and measured behavior of Gloucester clay versus specimen orientation during CIU triaxial compression tests (Lab data from [16]). (a) Stress-strain curves and (b) Excess pore pressures.

5. EVALUATION

5.1. Calculated and measured response—Gloucester clay

CRS CIU triaxial compression tests were performed on specimens of Gloucester clay [16] trimmed at 0°, 30°, 45°, 60° and 90° to the vertical. Figure 11 compares: (i) the measured and calculated

DOI: 10.1002/nag

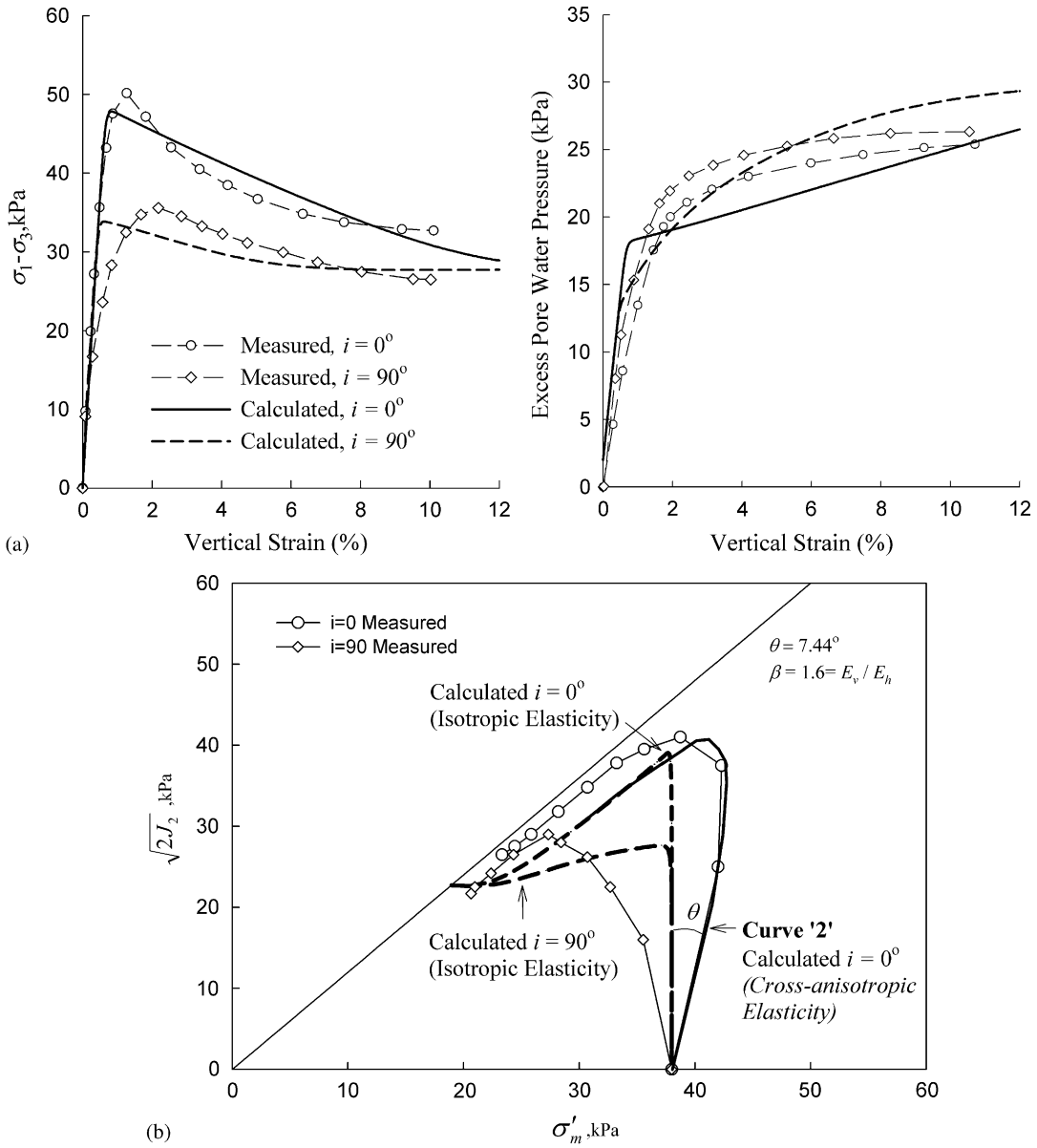

Figure 13. Improved agreement between calculated and measured excess pore pressure using cross-anisotropic elasticity for Gloucester clay (Lab data from [16]). (a) Stress-strain curves and excess pore pressures and (b) Stress path.

peak undrained shear strength versus sample orientation, i, (ii) measured and calculated post-peak strength at 8% axial strain, and (iii) the calculated intrinsic strength at 20% axial strain. The intrinsic strength was assumed in the FE interpretation even though it is difficult to reach such a state in a triaxial apparatus.

DOI: 10.1002/nag

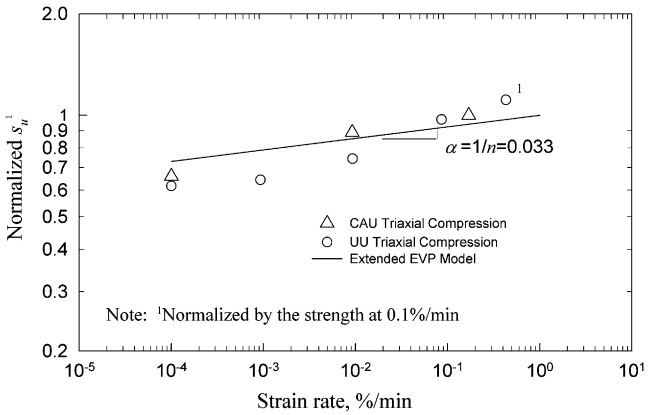

Figure 14. The influence of strain-rate on calculated and measured undrained shear strength of Gloucester clay (Lab data from [16]).

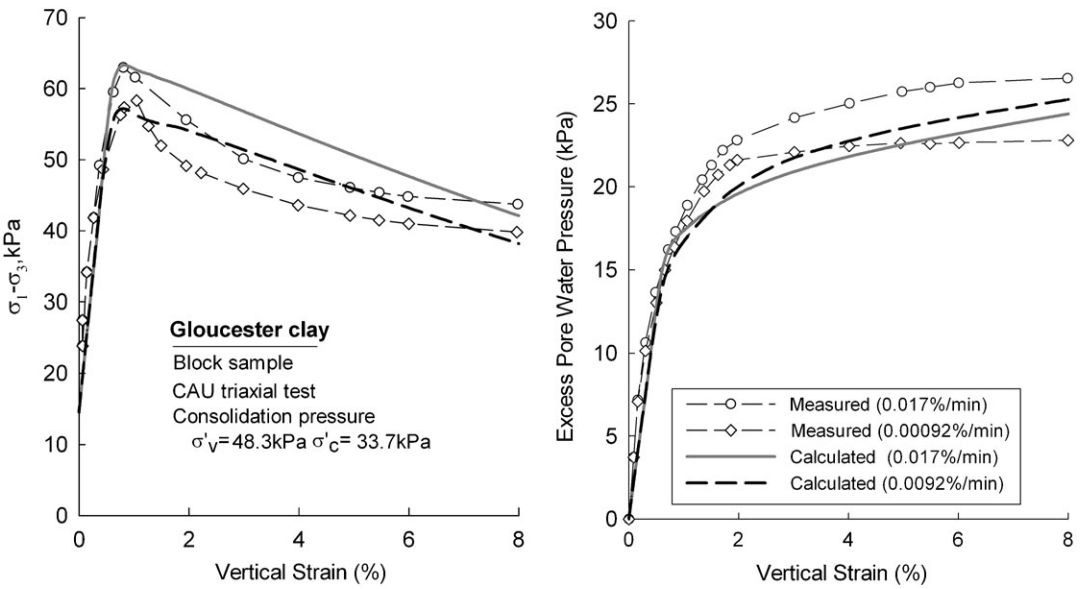

Figure 15. The influence of strain-rate during CAU triaxial tests on Gloucester clay (Lab data from (16)).

Referring to Figure 11, it can be seen that both the measured and calculated peak undrained shear strength of Gloucester clay are strongly anisotropic. In general, the peak strength of vertical specimens ($i = 0°$) is typically 40% higher than for horizontal specimens ($i = 90°$). At the peak strength, there is good agreement between the calculated (solid lines) and measured (symbols) undrained shear strength versus i. At an axial strain of 8%, the measured strength of Gloucester clay is only slightly lower than the calculated strength for all values of i. At the intrinsic state, which is reached at 20% axial strain (assumed), the theoretical strength of Gloucester clay is

DOI: 10.1002/nag

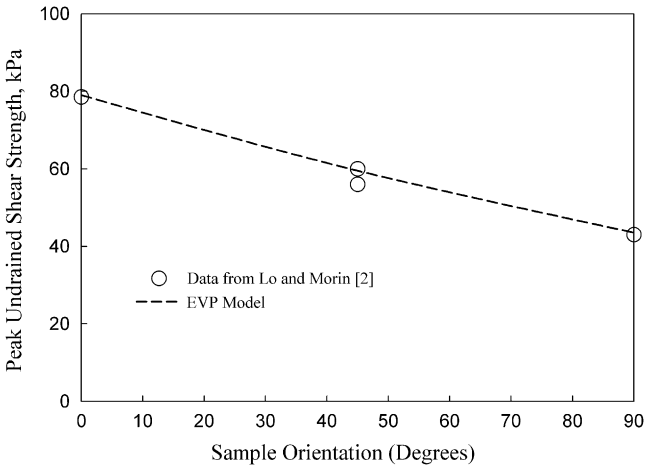

Figure 16. Calculated and measured peak undrained shear strength of St. Vallier clay during CIU triaxial tests versus sample orientation, i (Data from [2]).

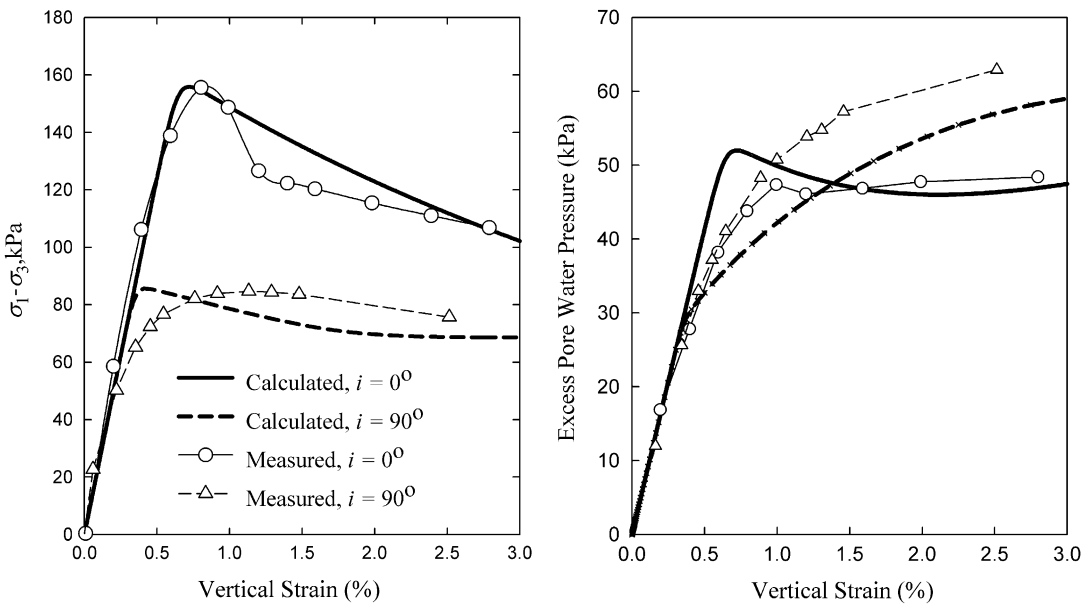

Figure 17. Response of vertical and horizontal specimens of St. Vallier clay (Data from [2]).

isotropic. In general, Figure 11 shows reasonable agreement between the calculated and measured variation of peak and post-peak strength for all sample orientations, i.

Figure 12 compares the calculated and measured (i) deviator stress ($q = \sigma_1 - \sigma_3$) versus axial strain and (ii) excess pore pressure versus axial strain corresponding to the test results summarized in Figure 4 (see also Table I). Figure 13 focuses on the behavior of vertical ($i = 0°$) and horizontal

DOI: 10.1002/nag

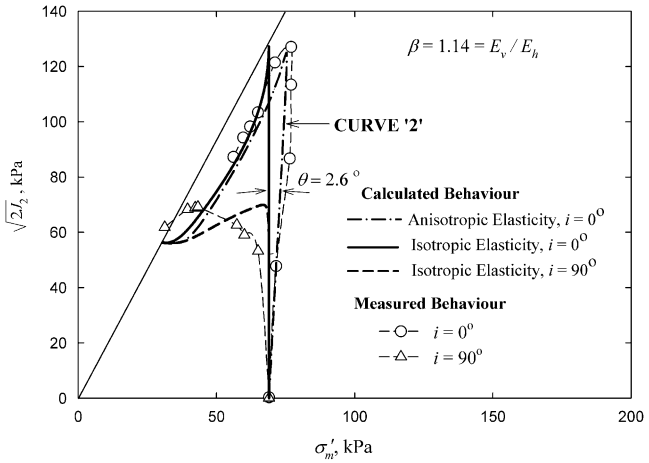

Figure 18. Calculated and measured stress paths for vertical and horizontal specimens of St. Vallier clay (Data from [2]).

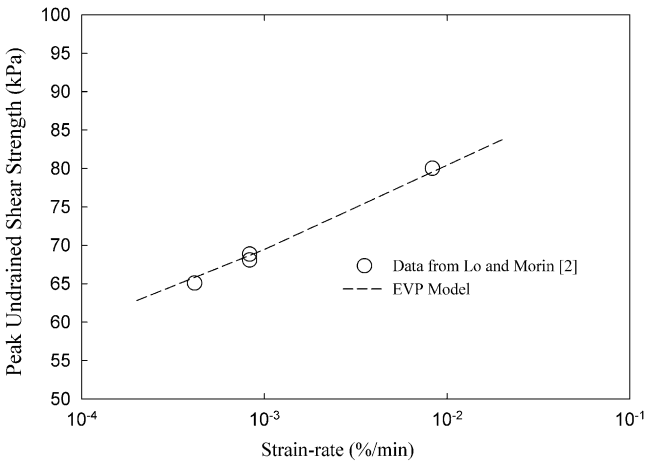

Figure 19. Calculated and measured undrained shear strength of St. Vallier clay versus strain-rate (Data from [2]).

specimens ($i = 90°$) and shows the corresponding stress paths. Referring first to Figure 12, the general agreement between measured and calculated behavior during CIU triaxial compression tests is considered to be adequate. The main differences between measured and calculated behavior are: (i) the measured rate of strain-softening is higher than the calculated rate for specimens trimmed at i of 0° and 30° and (ii) there are differences in the order of 15% between measured and calculated excess pore pressures in the elastic stress range. The latter is best seen by comparing the calculated and measured stress paths in Figure 13(b). In spite of these differences, the theoretical response is considered to be reasonable notwithstanding the impact of natural variation on the measured

DOI: 10.1002/nag

response. However, as discussed below in reference to Figure 13, it is possible to improve the calculated behavior by using cross-anisotropic elastic theory.

Referring to Figure 13, in accordance with Graham and Houlsby [50], an anisotropic elastic parameter, $\beta = E_v/E_h$, can be derived from deviation of the stress path from the vertical isotropic stress path for $i = 0°$. Notably, E_v and E_h are the vertical and horizontal elastic modulus, respectively. For Gloucester clay, the anisotropic elastic parameter, β, is approximately 1.6 assuming Poisson's ratio is 0.3. Subsequent, re-analysis of the CIU triaxial tests using cross-anisotropic elastic theory in the EVP model gives the stress path labeled Curve '2' in Figure 13(b), where it can be seen that accounting for cross-anisotropic elasticity produces a calculated stress path that is very close to that measured during CRS CIU triaxial compression for $i = 0°$. The deviator stress versus axial strain response is not significantly changed by adopting anisotropic elastic parameters.

To conclude, Figures 14 and 15 summarize the effect of strain-rate on the stress-strain and pore pressure response of Gloucester clay during CRS triaxial compression tests. Figure 14 compares calculated and measured undrained shear strength versus strain-rate. The measured response was obtained from a combination of UU and CAU triaxial tests on specimens from different depths. Thus, in order to compare the results, s_u has been normalized by the corresponding s_u undrained at the highest available strain-rate. Figure 15 shows the stress-strain response and stress path from the CAU tests, only. From Figures 14 and 15, it can be seen that the constitutive model is able to describe the general influence of strain-rate on the undrained strength, stress-strain response and stress paths for vertical specimens ($i = 0°$), which is considered to be encouraging. It is noted that the model has also been confirmed in Reference [12] for St. Jean Vianney clay from Eastern Canada for $i = 0°$.

5.2. Calculated and measured response—St. Vallier clay

In addition to Gloucester clay, the anisotropic behavior of St. Vallier clay is also examined. The behavior of St Vallier clay was reported by Lo and Morin [2] and Figures 16–19 compare calculated and measured behavior. The constitutive parameters for this case are summarized in Table IV.

Referring to Figure 16, it can be seen that the undrained shear strength of St. Vallier clay is also anisotropic. The peak undrained shear strength of vertical specimens, $i = 0°$, is about 80% higher than that of horizontal specimens ($i = 90°$), which is a significant difference. The EVP constitutive model is able to account for this anisotropy using $\Delta = 0.3$.

Figure 17 compares calculated and measured deviator stress and excess pore pressure versus axial strain for vertical and horizontal specimens. Results for other orientations can be found in Qu [21]. In general, the overall trends in the measured and calculated response presented in Figure 17 are considered to be consistent. Similar to Gloucester clay, there are slight differences between the measured and calculated excess pore water pressures, which can be attributed to the anisotropic elastic response of St. Vallier clay.

Figure 18 shows measured stress paths during CRS triaxial compression tests on specimens at $i = 0°$ and 90° and calculated stress paths using both isotropic and cross-anisotropic elasticity. For St. Vallier clay, the elastic anisotropic parameter, β, is 1.14. Similarly, Curve 2 in Figure 18 represents the calculated stress path corresponding to the use of cross-anisotropic elasticity in conjunction with the EVP model ($i = 0°$). Identical to that seen for Gloucester clay, there is improved agreement between calculated and measured stress paths if cross-anisotropic elasticity is assumed.

Finally, Figure 19 shows the effect of strain-rate on the measured and calculated undrained peak shear strength of St. Vallier clay. As shown in Figure 19, an order of magnitude increase in

DOI: 10.1002/nag

the applied strain-rate causes a 15% increase in the peak undrained shear strength of St. Vallier clay. In comparison, the peak strength of Gloucester clay increased by only 10% for an order of magnitude increase in the applied strain-rate. The increased rate-sensitivity is accounted for in the EVP model by decreasing the power law exponent, n, in (8) for St. Vallier clay (see Tables III and IV). The results in Figure 19 further highlight the significant influence of strain-rate on the engineering behavior of soft-sensitive clays from Eastern Canada.

5.3. Discussion

Based on the above comparisons, it has been shown that the extended EVP constitutive model is capable of describing: (i) the variation of peak and post-peak undrained shear strength as a function of sample orientation and (ii) the effects of strain-rate on the mobilized undrained shear strength of two structured clays from Eastern Canada. Both clays exhibit significant anisotropy at the peak strength but limited anisotropy at the large-strain post-peak state. For Gloucester clay and St. Vallier clay, the peak strength of vertical specimens is 40 and 80% higher, respectively, than the corresponding peak strength of horizontal specimens. Thus, the effects of anisotropy are significant and should be accounted for in the analysis of the clay behavior. In addition, the undrained strength of Gloucester and St. Vallier clay varies by 10 and 15% per order of magnitude change in the strain-rate, respectively. This is significant, and according to Marquis *et al.* [51] should be accounted for in engineering analyses. The extended EVP model permits consideration of both effects. Lastly, for both clays, the stress path measured during CIU triaxial compression tests could be simulated with good accuracy if anisotropic elasticity was used in conjunction with the structured EVP model.

6. GENERAL RESPONSE OF THE MODEL

The preceding sections described a structured EVP constitutive model and compared the calculated and measured behavior of two rate-sensitive structured clays from Eastern Canada. The comparisons demonstrated the ability of the model to describe the rate-sensitivity and anisotropy of two structured clays at failure. As noted in Section 3.4, however, the simplified constitutive model has two limitations which will be explored below by examining the influence of strain-rate on yielding in addition to the general response of the model for CAU triaxial compression and extension.

6.1. Yielding

Figure 20 shows a series of yield loci that have been derived from the EVP model using constitutive parameters listed in Table V for St. Alban clay [3]. The theoretical yield loci were derived assuming drained stress-path probes at axial strain-rates of 10^{-6}, 10^{-5} and $10^{-4}\%/\min$ along stress paths following stress ratios, $\eta = \sqrt{2J_2}/\sigma'_m$, between 0 and M_c.

Referring to Figure 20, it can be seen that the EVP model defines a series of yield loci that expand in stress space with increasing strain-rate. The spacing of the yield loci on the $\sigma'_m - \sqrt{2J_2}$ plane is governed by $\alpha = 1/n$ (see Figure 9); whereas, ω_o, and Δ govern the degree of distortion of the yield loci on the $\sigma'_m - \sqrt{2J_2}$ plane. Since μ_i and μ_s are isotropic and anisotropic, respectively, the EVP model defines three distinct ranges of behavior; notably: (i) For strain-rates greater than $1/\mu_i$, the dynamic yield loci plot as a unique curve when normalized by $\sigma'^{(d)}_{my}$ (Figure 21); (ii) For strain-rates less than $1/\mu_s$, the yield locus becomes isotropic and elliptical governed by (3);

DOI: 10.1002/nag

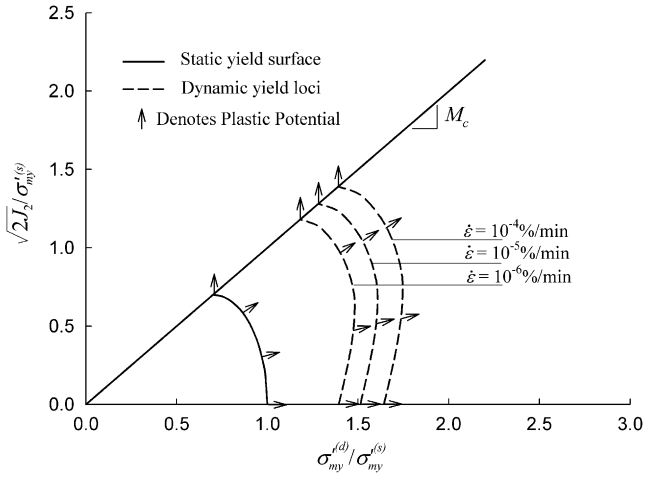

Figure 20. Derived yield loci versus strain-rate from the EVP model.

Table V. Constitutive parameters for parametric study.

Parameter	Value
Initial void ratio, e	2.4
Damage exponent, α_d	0.3
Static Yield Surface Intercept $\sigma'^{(s)}_{my}$, (kPa)	17
Visoplastic strain-rate exponent, n	28
Permeability, (cm/sec)	8.0×10^{-8}
M_c	1.0
Poisson's ratio, v	0.3
Recompression index, κ	0.07
Compression index, λ	0.75
Aspect ratio of elliptical cap, R	0.45
A (weighting parameter)	0.5
Δ	1.3
Structured viscosity, μ_s, (s)	6.6×10^{13}
Intrinsic viscosity, μ_i, (s)	4.6×10^{11}
Elastic anisotropy parameter, $\beta = E_v/E_h$	1.18

and (iii) There is a transition from isotropic to anisotropic yield curves for strain rates between $1/\mu_s$ and $1/\mu_i$, respectively. Figures 9(b) and (d) also illustrate the strain-rate effects noted above on the structure reflected in (13) and (14) for CRS triaxial and oedometer compression. As a result, it can be seen that the modeled structure has some rate dependency, which is consistent with the experimental results summarized in References [2] and [29]. However, if rate-independent structure is required, then μ_i and μ_s can be set sufficiently low to maintain constant structure and anisotropy for all strain-rates of practical engineering significance.

Secondly, as noted in Section 3, the plastic strain increment vector is isotropic since it is derived from (3); The corresponding plastic strain increment vectors are plotted in Figure 20.

DOI: 10.1002/nag

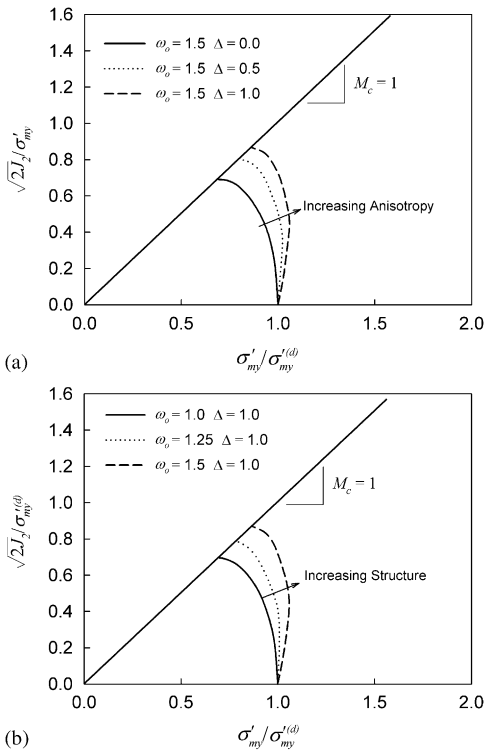

Figure 21. The effect of structure and anisotropy on the shape of yield loci derived from the EVP model. (a) Increasing anisotropy and (b) Increasing structure.

Based on Figure 20, it can be seen that the strain increment vectors appear to be non-associated when referenced to the dynamic yield loci for strain-rates between 10^{-4} and $10^{-6}\%/min$. The implications of such an assumption are unknown; however, the impact is expected to be small and insignificant for constant volume shear failure at the critical state and more significant for stress paths such as K_o compression that result in yielding.

Finally, Figure 21 summarizes the influence of structure, ω_o, and anisotropy, Δ, on derived normalized yield loci corresponding to strain-rates greater than $1/\mu_i$. Figure 21(a) illustrates the influence of anisotropy as reflected in the parameter Δ; whereas, Figure 21(b) illustrates the influence of structure, which is reflected in the parameter ω_o. Referring to Figure 21(a), keeping the structure constant, $\omega = 1.5$, and increasing Δ from 0 to 0.5 causes the derived yield loci to become more distorted on the $\sigma'_m - \sqrt{2J_2}$ plane. For $\Delta = 0$, the yield surface is elliptical and centered on the σ'_m - axis; whereas, for $\Delta = 0.5$, the yield locus is distorted similar to Curve I in Figure 5.

Similarly, for constant anisotropy, $\Delta = 0.5$, increasing the structure from 0 to 1.5 causes increasing distortion of the apparent yield surfaces on the $\sigma'_m - \sqrt{2J_2}$ plane (Figure 21(b)). From Figure 21(b), it can be seen that given $\Delta = 0.5$, destructuration (decreasing ω) causes the yield surface to become less distorted on the $\sigma'_m - \sqrt{2J_2}$ plane eventually reaching an elliptical shape centered on the mean stress axis, which is comparable to the behavior of St. Alban clay (Figure 5).

DOI: 10.1002/nag

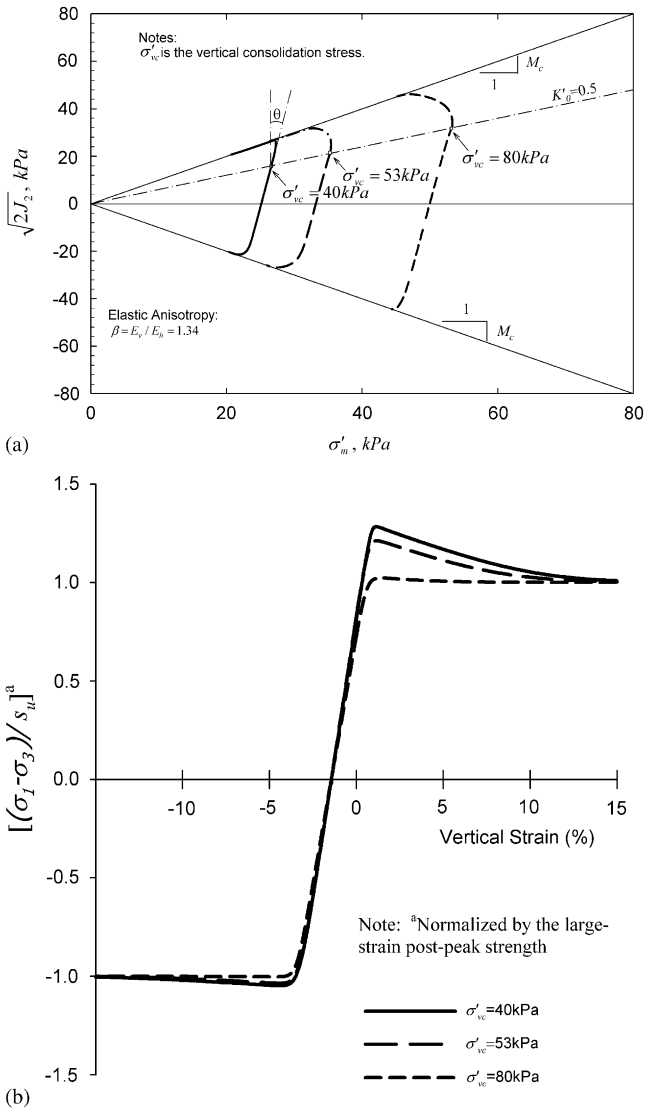

Figure 22. Response of the extended EVP model during CAU triaxial compression and extension for parmameters corresponding to St. Alban clay [3, 25]. (a) Stress paths and (b) Normalized stress-strain response.

6.2. CAU triaxial compression and extension

To conclude, the response of the model for CAU triaxial extension and compression is shown in Figures 22 and 23. The results presented in these figures were obtained by performing FE analyses using (i) the constitutive parameters listed in Table V and (ii) cross-anisotropic elasticity. Three separate CAU triaxial compression and extension tests were numerically simulated assuming each specimen was consolidated anisotropically ($K_o = 0.5$) to vertical stresses of 40, 53 and 80 kPa,

DOI: 10.1002/nag

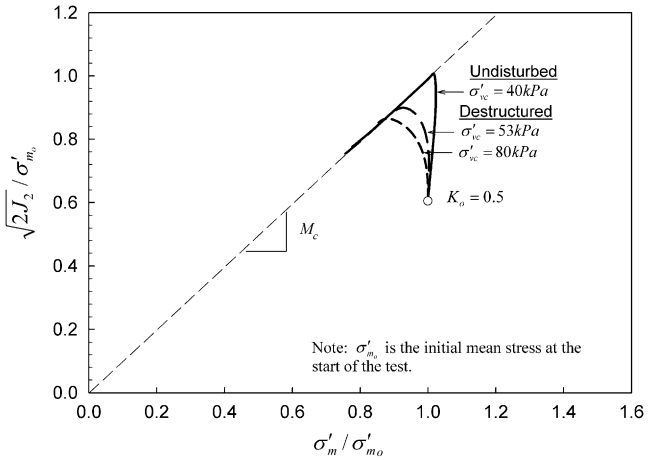

Figure 23. Normalized stress paths during CAU triaxial compression for parameters corresponding to St. Alban clay [3, 25].

corresponding to volumetric strains of 3, 8 and 20%. Similar to that described above, the FE program AFENA [49] was used to simulate these tests. The FE simulations involved modeling anisotropic consolidation for 24 h followed by undrained triaxial compression or extension. Figure 22 shows the stress-strain and stress path during the simulated tests.

From Figure 22, it can be seen that the ratio of peak to post-peak strength decreases with increasing volumetric strain during the consolidation phase. In addition, a series of stress paths are predicted by the model inclined by angle θ relative to vertical due to the use of cross-anisotropic elastic theory. Figure 22 illustrates the main limitation of the EVP model, which is the model predicts the same stress ratio at failure for compression and extension, whereas, clay is typically weaker in extension than in compression (see Figure 10). In addition, the model neglects induced anisotropy. Figure 23 shows the corresponding normalized stress paths during compression. As discussed in Section 2, the behavior depicted in Figure 23 has been observed for Bothkenar clay [26] and Leirstranda and OnsØy clays [27] due to sample disturbance, which is known to destructure clay.

7. SUMMARY AND CONCLUSIONS

This paper has described a constitutive approach for modeling the rate-dependent, anisotropic behavior of structured clay. The foundation of the constitutive approach is an existing overstress EVP model [8, 9], which has been extended by Hinchberger and Qu [12] using a state-dependent viscosity parameter to account for the effects of clay structure. In this paper, a tensor approach similar to that described by Boehler [13], Pietruszczak and Mroz [14] and Cudny and Vermeer [15] has been used to incorporated anisotropic viscoplasticity into the model, which has been shown to describe some of the key engineering characteristics of two clays from Eastern Canada.

DOI: 10.1002/nag

Based on the analyses and discussions presented above, the following observations and conclusions can be made:

1. The anisotropic structured EVP model can describe the effect of strain-rate and sample orientation on the peak and post-peak undrained shear strength of Gloucester and St. Vallier clay. This is considered to be new and should be useful in modeling the response of soft viscous structured clays.
2. The new constitutive approach assumes that the post-peak strength during CIU triaxial compression is isotropic, which is consistent with the behavior of Gloucester clay reported in Figure 4 and Table I [16].
3. The peak strength of St. Vallier clay is more anisotropic ($\Delta = 0.3$) than that of Gloucester clay ($\Delta = 0.15$). For Gloucester clay, the peak strength was 40% higher than the large-strain post-peak strength; whereas, for St. Vallier clay, the peak strength was 80% higher than the post-peak strength. In contrast, the opposite was observed for the elastic anisotropy where $\beta = 1.6$ for Gloucester clay compared to $\beta = 1.15$ for St. Vallier clay. As a result, it is concluded that the degree of elastic and viscoplastic anisotropy are not necessarily interrelated for structured clay.
4. The anisotropic EVP model defines a series of strain-rate-dependent yield loci that appear to be rotated on the $\sigma'_m - \sqrt{2J_2}$ plane for the undisturbed material. After destructuration, however, the resultant yield loci is elliptical and centered on the σ'_m-axis similar to that seen for St. Alban clay (Figure 5) and some other structured clays, which have a high void ratio and liquidity index.
5. For Gloucester clay, it is concluded that both cross-anisotropic elasticity and anisotropic viscoplasticity should ideally be accounted for in a constitutive model for this material. For St. Vallier clay, the need to account for the anisotropic elasticity is less evident; however, strain-rate effects and structure are significant.
6. The EVP constitutive model has two limitations: (i) The yield surface and critical state functions are isotropic and possess a circular trace on deviatoric planes. This can have implications for the analysis of plane strain problems and should be taken into account by averaging compression and extension test results to obtain the slope of the critical state line. (ii) The plastic potential is also isotropic in spite of the anisotropic strength. The implication of this limitation has not been explored; however, it is considered to be minor at the critical state and more important for compression along stress paths other than the critical state.
7. Lastly, since the model neglects induced anisotropy, it should not be used for cases were induced anisotropy plays a more important role than strain-rate effects and destructuration.

APPENDIX A

A relationship for can be derived from the EVP constitutive equations as described below. First, from (3) representing the elliptical cap, it can be shown that

$$s_{u_p} = \chi \sigma'^{(d)}_{my_p} \tag{A1}$$

where s_{u_p} and $\sigma'^{(d)}_{my_p}$ are the undrained shear strength and dynamic yield surface intercept corresponding to the peak state, the subscript p denotes conditions corresponding to the peak strength and χ is a constant ($= M_c/(M_c R + 1)$). At yield and failure, the elastic strain-rate tensor

DOI: 10.1002/nag

can be neglected since $\dot{\varepsilon}_{ij}^{vp} \gg \dot{\varepsilon}_{ij}^{e}$ and the EVP constitutive equation corresponding to the peak strength is

$$\dot{\varepsilon}_{11} = \frac{1}{\mu_s}[(\sigma'^{(d)}_{my_p}/\sigma'^{(s)}_{my_p})^n - 1]\frac{\partial F}{\partial \sigma'_{11}} = \frac{1}{\mu_s}[(s_{u_p}/\chi\sigma'^{(s)}_{my_p})^n - 1]\frac{\partial F}{\partial \sigma'_{11}}. \tag{A2}$$

where $\dot{\varepsilon}_{11}$ is the axial strain-rate, σ'_{11} is the effective axial stress, and all other notation is defined in the paper. Similarly, the EVP equation governing the large-strain post-peak strength is

$$\dot{\varepsilon}_{11} = \frac{1}{\mu_i}[(s_{u_i}/\chi\sigma'^{(s)}_{my_i})^n - 1]\frac{\partial F}{\partial \sigma'_{11}}, \tag{A3}$$

where the subscript i denotes the intrinsic state. Dividing (A2) by (A3) and rearranging gives

$$\frac{\mu_s}{\mu_i} = \frac{(s_{u_p}/\chi\sigma'^{(s)}_{my_p})^n - 1}{(s_{u_i}/\chi\sigma'^{(s)}_{my_i})^n - 1} \cong \frac{(s_{u_p}/\sigma'^{(s)}_{my_p})^n}{(s_{u_i}/\sigma'^{(s)}_{my_i})^n}, \tag{A4}$$

which for typical values of μ_s, μ_i and n is accurate for (a) the strain-rates used during laboratory tests and (b) soils that reach the peak and large-strain post-peak states at approximately the same stress ratio ($\eta = \sqrt{2J_2}/\sigma'_m$). Finally, strain hardening of the static yield surface can be neglected without introducing significant error (e.g. $\sigma'^{(s)}_{my_p} = \sigma'^{(s)}_{my_i}$) leading to

$$\omega_o = \left(\frac{\mu_s}{\mu_i}\right)^{1/n} = \frac{s_{u_p}}{s_{u_i}}. \tag{A5}$$

An equation relating ω_o to the structured, σ'_{p_s}, and intrinsic, σ'_{p_i}, preconsolidation pressures (Figure 9) can be derived using the same approach; Notably, for the elliptical cap yield surface, there is a fixed ratio between the preconsolidation pressure, σ'_p, and the yield surface intercept, viz.

$$\sigma'_p = X\sigma'^{(d)}_{my}, \tag{A6}$$

where X is a constant of proportionality. Substituting (A6) evaluated for the structured, σ'_{p_s}, and intrinsic, σ'_{p_i}, preconsolidation pressures into the EVP constitutive equations and following the approach described above for the undrained shear strength leads to

$$\omega_o = \left(\frac{\mu_s}{\mu_i}\right)^{1/n} = \frac{\sigma'_{p_s}}{\sigma'_{p_i}}. \tag{A7}$$

NOTATION

$\dot{\varepsilon}_{ij}$ strain-rate tensor
$\dot{\varepsilon}_{ij}^{e}$ elastic strain-rate tensor
$\dot{\varepsilon}_{ij}^{vp}$ viscoplastic strain-rate tensor
$\dot{\varepsilon}_{11}$ axial strain-rate

DOI: 10.1002/nag

σ'_{ij}, s_{ij}	effective stress tensor and deviatoric stress tensor
σ'_m	mean effective stress, $(\sigma'_1+\sigma'_2+\sigma'_3)/3$
J_2	second invariant of the deviatoric stress tensor $\frac{1}{6}[(\sigma'_{11}-\sigma'_{22})^2+(\sigma'_{22}-\sigma'_{33})^2]+\sigma'^2_{11}+\sigma'^2_{23}+\sigma'^2_{31}$
K_o	coefficient of lateral earth pressure at rest
δ_{ij}	Kronecker's delta
E	Young's modulus
K, G	elastic bulk and shear modulus
v	Poisson's ratio
E_v, E_h	vertical and horizontal elastic Young's modulus
β	cross-anisotropic elastic parameter, E_v/E_h
κ, λ	recompression and compression indices
e	void ratio
μ, n	viscosity and power law exponent
μ_s	viscosity of structured clay fabric
μ_i	viscosity of the intrinsic clay fabric
M_c	slope of the critical state line
R	aspect ratio (elliptical cap)
l	σ'_m and $\sqrt{2J_2}$- coordinates at the top of the cap
$\sigma'^{(s)}_{my}$, $\sigma'^{(d)}_{my}$	static and dynamic yield surface intercepts.
c	tension intercept (dynamic yield surface only)
$\phi(F)$	flow function
$[\partial F/\partial\sigma'_{ij}]$	plastic potential
s_u	undrained shear strength
σ'_p	preconsolidation pressure
ω_o	initial structure parameter
$\omega(\varepsilon_d, \eta^*)$	state-dependent structure parameter
α_d	parameter controlling the rate of destructuration
ε_d, A	damage strain and weighting parameter for calculating ε_d
ε^{vp}_{vol}, ε^{vp}_s	viscoplastic volumetric and octahedral shear strains
M_{oc}	slope of the failure envelop in the over-consolidated stress range
s_{u_p}, s_{u_i}	structured and instrinsic undrained shear strength
$\sigma'_{ps}, \sigma'_{pi}$	structured and intrinsic preconsolidation pressure
Δ	anisotropic constitutive parameter
η^*	anisotropic scalar parameter (derived)
η	stress ratio $(=\sqrt{2J_2}/\sigma'_m)$
a^T_{ij}	microstructure tensor
C_α, C_r, C_c	coefficient of secondary compression, and recompression and virgin compression indexes
q	deviator stress $(=\sigma_1-\sigma_3)$

ACKNOWLEDGEMENTS

The research reported in this paper was funded by research grants held by Drs. Hinchberger and Lo and obtained from the Natural Sciences and Engineering Research Council of Canada.

DOI: 10.1002/nag

REFERENCES

1. Vaid YP, Robertson PK, Campanella RG. Strain rate behaviour of Saint-Jean-Vianney clay. *Canadian Geotechnical Journal* 1979; **16**(1):35–42.
2. Lo KY, Morin JP. Strength anisotropy and time effects of two sensitive clays. *Canadian Geotechnical Journal* 1972; **9**(3):261–277.
3. Tavenas F, Leroueil S, La Rochelle P, Roy M. Creep behaviour of an undisturbed lightly overconsolidated clay. *Canadian Geotechnical Journal* 1978; **15**(3):402–423.
4. Lo KY. Stability of slopes in anisotropic soils. *Journal of the Soil Mechanics and Foundations Division* (ASCE) 1965; **91**(SM4):85–106.
5. Mitchell JK. *Foundamental of Soil Behaviour*. Wiley: New York, 1976.
6. Leroueil S, Vaughan PR. The general and congruent effects of structure in natural soils and weak rock. *Geotechnique* 1990; **40**(3):467–488.
7. Burland JB. On the compressibility and shear strength of natural clays. *Geotechnique* 1990; **40**(3):329–378.
8. Hinchberger SD, Rowe RK. Modelling the rate-sensitive characteristics of the Gloucester foundation soil. *Canadian Geotechnical Journal* 1998; **35**(5):769–789.
9. Hinchberger SD. The behaviour of reinforced and unreinforced embankments on rate sensitive clayey foundations. *Department of Civil Engineering*, University of Western Ontario, London, 1996.
10. Perzyna P. Constitutive equations for rate sensitive plastic materials. *Quarterly of Applied Mathematics* 1963; **20**(4):321–332.
11. Chen WF, Mizuno E. *Nonlinear Analysis in Soil Mechanics*: *Theory and Implementation*. Elsevier Science Publishing Company Inc.: New York, NY, U.S.A., 1990.
12. Hinchberger SD, Qu G. A viscoplastic constitutive approach for structured rate-sensitive natural clay. *Canadian Geotechnical Journal* 2008; **46**(7):609–626.
13. Boehler JP. *Applications of Tensor Functions in Solid Mechanics*. Springer: Wien, 1987.
14. Pietruszczak S, Mroz Z. On failure criteria for anisotropic cohesive-frictional materials. *International Journal for Numerical and Analytical Methods in Geomechanics* 2001; **25**(5):509–524.
15. Cudny M, Vermeer PA. On the modelling of anisotropy and destructuration of soft clays within the multi-laminate framework. *Computers and Geotechnics* 2004; **31**(1):1–22.
16. Law KT. *Analysis of Embankments on Sensitive Clays*, *in Faculty of Engineering Science*. University of Western Ontario, London, Ontario, 1974.
17. Lefebvre G. Fourth Canadian geotechnical colloquium. Strength and slope stability in Canadian soft clays deposits. *Canadian Geotechnical Journal* 1981; **18**:420–442.
18. Kulhawy FH, Mayne PW. *Manual on Estimating Soil Properties for Foundation Design*. Electric Power Research Institute: Palo Alto, CA, 1990.
19. Graham J, Crooks JHA, Bell AL. Time effects on the stress-strain behaviour of natural soft clays. *Geotechnique* 1983; **33**(3):327–340.
20. Qu G, Hinchberger SD, Lo KY. Evaluation of the viscous response of clay using generalized elastic viscoplastic theory. *Geotechnique* 2009; accepted.
21. Qu G. Selected issues on the performance of embankments on clay foundations. *Civil and Environmental Engineering Department*. University of Western Ontario, London, 2008.
22. Hinchberger S, Qu GF. Discussion: influence of structure on the time-dependent behaviour of a stiff sedimentary clay. *Geotechnique* 2007; **57**(9):783–787.
23. Lo KY, Milligan V. Shear strength properties of two stratified clays. *American Society of Civil Engineers Proceedings*, *Journal of the Soil Mechanics and Foundations Division American Society of Civil Engineers* 1967; **93**(SM1):1–15.
24. Ladd CC. 22nd Terzaghi Lecture: Stability evaluation during staged construction. *ASCE Journal of Geotechnical Engineering* 1991; **117**(4):540–615.
25. Leroueil S, Tavenas F, Brucy F, La Rochelle P, Roy M. Behavior of destructured natural clays. *Journal of the Geotechnical Engineering Division* 1979; **105**(6):759–778.
26. Smith PR, Jardine RJ, Hight DW. Yielding of Bothkennar clay. *Geotechnique* 1992; **42**(2):257–274.
27. Lunne T, Berre T, Andersen KH, Strandvik S, Sjursen M. Effects of sample disturbance and consolidation procedures on measured shear strength of soft marine Norwegian clays. *Canadian Geotechnical Journal* 2006; **43**(7):726–750.
28. Sheahan TC. Interpretation of undrained creep tests in terms of effective stresses. *Canadian Geotechnical Journal* 1995; **32**:373–379.

DOI: 10.1002/nag

29. Vade YP, Campanella RG. Time dependent behaviour of undisturbed clay. *ASCE Journal of Geotechnical Engineering* 1977; **GT7**(2):693–709.
30. Leroueil S, Samson L, Bozozuk M. Laboratory sand field determination of preconsolidation pressures at Gloucester. *Canadian Geotechnical Journal* 1983; **20**(3):477–490.
31. Vermeer P, Neher HP. A soft soil model that accounts for creep. *Proceedings of the International Symposium*: *Beyond 2000 in Computational Geotechnics*, Amsterdam, Maray 1999; 249–261.
32. Yin J-H, Graham J. Elastic viscoplastic modelling of the time-dependent stress-strain behaviour of soils. *Canadian Geotechnical Journal* **36**:736–745.
33. Adachi T, Oka F. Constitutive equations for normally consolidated clay based on elasto-viscoplasticity. *Soils and Foundations* 1982; **22**(4):57–70.
34. Roscoe KH, Burland JB. On the generalised stress-strain behaviour of wet clay. In *Engineering Plasticity*. Heyman J, Leckie FA (eds). Cambridge University Press: Cambridge, 1968; 535–609.
35. Roscoe KH, Schofield AN, Thurairajah A. Yielding of clays in states wetter than critical. *Geotechnique* 1963; **13**(3):211–240.
36. Desai CS, Somasundaram S, Frantziskonis G. A hierarchical approach for constitutive modelling of geologic materials. *International Journal for Numerical and Analytical Methods in Geomechanics* 1986; **10**(3):225–257.
37. Leroueil S. The isotach approach. Where are we 50 years after its development by Professor Suklje. *Proceedings of the XIII Danube-European Conference on Geotechnical Engineering*, Ljubljana, Slovenia, vol. 1, 2006; 55–88.
38. Rouainia M, Wood DM. Kinematic hardening constitutive model for natural clays with loss of structure. *Geotechnique* 2000; **50**(2):153–164.
39. Nova R, Castellanza R, Tamagnini C. A constitutive model for bonded geomaterials subject to mechanical and/or chemical degradation. *Internatinal Journal for Numerical and Analytical Methods in Geomechanics* 2003; **27**(3):705–732.
40. Lade PV. Failure criterion for cross-anisotropic soils. *ASCE Journal of Geotechnical and Geoenvironmental Engineering* 2008; **134**(1):117–124.
41. Grammatikopoulou A, Zdravkovic L, Potts DM. The effect of the yield and plastic potential deviatoric surfaces on the failure height of an embankment. *Geotechnique* 2007; **57**(10):795–806.
42. Whittle AJ, Kavvadas MJ. Formulation of MIT-E3 constitutive model for overconsolidated clays. *Journal of Geotechnical Engineering* 1994; **120**(1):173–198.
43. Wheeler SJ, Näätänen A, Karstunen M, Lojander M. An anisotropic elastoplastic model for soft clays. *Canadian Geotechnical Journal* 2003; **40**(2):403–418.
44. Davies MCR, Newson TA. Critical state constitutive model for anisotropic soil. *Proceedings of the Wroth Memorial Symposium*. Published by Thomas Telford Services Ltd: Oxford, UK, London, England, 1992.
45. Tobita Y, Yanagisawa E. Modified stress tensors for anisotropic behavior of granular materials. *Soils and Foundations* 1992; **32**:85–99.
46. Miura K, Miura S, Toki S. Deformation behaviour of anisotropic dense sand under principal stress axes rotation. *Soils and Foundations* 1986; **26**:36–52.
47. Tobita Y. Yield condition of anisotropic granular materials. *Soils and Foundations* 1988; **28**:113–126.
48. Sun DA, Matsuoka H, Yao YP. An anisotropic hardening elastoplastic model for clays and sands and its application to FE analysis. *Computers and Geotechnics* 2004; **31**:37–46.
49. Carter JP, Balaam NP. AFENA-A general finite element algorithm: users manual. 1990, School of Civil Engineering and Mining Engineering, University of Sydney, Australia.
50. Graham J, Houlsby GT. Anisotropic elasticity of a natural clay. *Geotechnique* 1983; **33**(2):165–180.
51. Marques MES, Leroueil S, de Almeida M. Viscous behaviour of St-Roch-de-l'Achigan clay, Quebec. *Canadian Geotechnical Journal* 2004; **41**(1):25–38.

DOI: 10.1002/nag